Delay dynamics of neuromorphic optoelectronic nanoscale resonators: Perspectives and applications

Cite as: Chaos **27**, 114323 (2017); https://doi.org/10.1063/1.5008888
Submitted: 24 May 2017 . Accepted: 14 September 2017 . Published Online: 03 November 2017

Bruno Romeira, José M. L. Figueiredo, and Julien Javaloyes

Delay dynamics of neuromorphic optoelectronic nanoscale resonators: Perspectives and applications

Bruno Romeira,[1,a),b)] José M. L. Figueiredo,[1,c)] and Julien Javaloyes[2]
[1]*Centro de Electrónica, Optoelectrónica e Telecomunicações (CEOT), Departmento de Física, Universidade do Algarve, Campus de Gambelas, 8005-139 Faro, Portugal*
[2]*Departament de Física, Universitat de les Illes Balears, C/Valldemossa km 7.5, 07122 Palma de Mallorca, Spain*

(Received 24 May 2017; accepted 14 September 2017; published online 3 November 2017)

With the recent exponential growth of applications using artificial intelligence (AI), the development of efficient and ultrafast brain-like (neuromorphic) systems is crucial for future information and communication technologies. While the implementation of AI systems using computer algorithms of neural networks is emerging rapidly, scientists are just taking the very first steps in the development of the hardware elements of an artificial brain, specifically neuromorphic microchips. In this review article, we present the current state of the art of neuromorphic photonic circuits based on solid-state optoelectronic oscillators formed by nanoscale double barrier quantum well resonant tunneling diodes. We address, both experimentally and theoretically, the key dynamic properties of recently developed artificial solid-state neuron microchips with delayed perturbations and describe their role in the study of neural activity and regenerative memory. This review covers our recent research work on excitable and delay dynamic characteristics of both single and autaptic (delayed) artificial neurons including all-or-none response, spike-based data encoding, storage, signal regeneration and signal healing. Furthermore, the neural responses of these neuromorphic microchips display all the signatures of extended spatio-temporal localized structures (LSs) of light, which are reviewed here in detail. By taking advantage of the dissipative nature of LSs, we demonstrate potential applications in optical data reconfiguration and clock and timing at high-speeds and with short transients. The results reviewed in this article are a key enabler for the development of high-performance optoelectronic devices in future high-speed brain-inspired optical memories and neuromorphic computing.
https://doi.org/10.1063/1.5008888

Our aim in this article is to provide a review of our recent achievements for readers who wish to study and emulate the biophysics of spiking neurons and dynamic synapses using advanced brain-inspired (neuromorphic) optoelectronic oscillators. In our approach, electronic and photonic elements converge towards one hybrid micro- nanotechnology, offering great advantages for implementing ultra-compact, high-speed, and low-power artificial brain-inspired microchips. First, after introducing the state of the art of neuromorphic electronic and photonic circuits, we summarize our experimental and theoretical work on neuromorphic optoelectronic resonators using solid-state resonant tunneling diode circuits integrated with high-speed detectors and light sources. These neuromorphic microchips can be activated either optically or electrically featuring a wide range of neuron-like signal outputs—spiking, bursting, periodic and aperiodic mixed mode oscillations—and other phenomena—e.g., coherence resonance (CR). Second, we review our work aiming at using these neuromorphic photonic circuits to build robust, flexible, and high-speed brain-inspired regenerative optical memories displaying the unique signatures of spatio-temporal localized structures of light.

I. INTRODUCTION

We are currently witnessing an exponential growth of artificial intelligence systems to help humans dealing with highly complex tasks, such as sensing and learning,[1–5] needed for the internet of things and to handle with big data. While conventional digital computing has been the engine of the information technology revolution in the past decades, this technology falls far short of the human brain in terms of problem-solving abilities and power consumption. For this reason, neural networks, i.e., collections of artificial neurons mimicking biological brain functions, are currently the focus of much attention. To this end, there is a strong focus not only on the development of deep neural networks using computer algorithms[6–8] but also in integrated neuromorphic microchips[5,9–11] as the hardware that can reproduce neurotransmission dynamics—the communication between neurons—by interconnecting many artificial neuron-like elements. This communication is encoded in sequences of intensity spikes

[a)]Electronic mail: bmromeira@ualg.pt.
[b)]Current address: International Iberian Nanotechnology Laboratory (INL), Av. Mestre José Veiga, Braga 4715-330, Portugal.
[c)]Current address: Departamento de Física, Faculdade de Ciências da Universidade de Lisboa, Campo Grande, 1749-016 Lisboa, Portugal.

(the excitable pulses[12]) as found in the unique information processing of the brain.

This challenging and highly interdisciplinary area of research has recently mobilized significant researchers around the world. In the United States, researchers funded by DARPA SyNAPSE developed a one million neuron brain-inspired processor,[13] the TrueNorth chip. In 2012, Intel announced their venture into neuromorphic chip development with a new architecture resulting in the start-up development of the QuarkSE chip. In Stanford University, the Neurogrid[14] implemented a mixed-analog-digital multi-chip system for large-scale neural simulations. In Europe, the FACETS program[15] developed a chip with 200 000 neurons and 50 million synaptic connections which in turn has led to the European initiative "The Human Brain Project" launched in 2014.[16] Other examples of projects in brain machine simulation include the SpiNNaker[17] and the BrainScaleS[18] initiatives.

Thus far, the emphasis has been on the development of neuromorphic electronic technologies based on CMOS and/or memristors.[9–11,19–21] Although the impressive advances, these approaches use electronic synapses[22] at kHz speeds, which are difficult to interface with optical technologies for implementation in the context of high-bandwidth optical communications systems. One of the most promising alternatives is to use light-based synapses enabled by neuromorphic photonic integrated chips. This approach takes advantage of energy efficient optical interconnects to achieve low-power neuron-like responses at speeds one billion times faster than neurons (>1 Gb/s). This is also much faster than the electronic-based artificial neurons, making optical neurons excellent candidates to realize the dream of a fully integrated brain-inspired photonic information processor. In photonics, high-speed neuromorphic spiking responses can be achieved using semiconductor lasers[23] and other optoelectronic-based configurations,[24,25] see a recent review in Ref. 26. Several laser-based neuromorphic systems have been proposed for telecommunication wavelengths (see, for example, the recent work of Hurtado *et al.*,[27] and references therein), and therefore compatible with current fiber-optic communication systems.

While considerable attention has been dedicated to the realization of optical neurons and network architectures, less attention has been paid to the mechanism of autaptic, i.e., self-feedback, connections in neurons. These synapses between a neuron and a branch of its own axon were reported for the first time more than four decades ago,[28] and have been found in the neocortex and the hippocampus regions of the brain, among other areas.[29] Several works suggest that these autaptic neural connections are abundant in specific types of neurons,[30] having key implications in synaptic transmission[31] and in local feedback neuron regulation.[29,32] In neural networks, these self-feedback connections may offer energetically effective means for controlling network dynamics towards specific states.[33,34] A number of theoretical studies show that the delays in autaptic inputs affect the bursting behavior and information transfer of individual neurons.[35–38] Despite the potential applications of autaptic neurons, excluding the work on reservoir computing that uses a single dynamical delayed node as a complex network to perform computation,[39] experimental autaptic neurons remain almost unexplored in the context of neuromorphic microchips.

In this article, we review our recent work on solid-state artificial neurons with autaptic (delayed) perturbations. In Fig. 1, we show a schematic diagram that compares the biological neuron, panels (a) and (b), with our solid-state neuron, panels (c) and (d). The biological neuron, panel (a), consists of a soma region (cell body nucleus), dendrites (thin structures that arise from the cell body), and axon terminals (a long cellular extension that arises from the cell body). Neurons generate action potentials (electrical spikes), with amplitudes of approximately 100 mV and duration in the range of 0.1–1 ms in their soma. The spikes then propagate through the axon and are transmitted to the next neuron through the synapses consuming less than 10 pJ per spike.[40] The synapses, which are 20–40 nm wide gaps between the axon end and the dendrites, transmit the signal either chemically by releasing neurotransmitters or electrically, depending on the type of the synapse. The typical performance of a biological neuron is detailed in the top left of Fig. 1. In panel (b), it is shown a schematic representation of an autaptic neuron with a self-feedback connection with a time-delay τ due to the presence of an autapse. These types of connections provide additional control of the synaptic activity of neurons.

The artificial neuron, panel (c), consists of a neuromorphic optoelectronic microchip[41] formed by two key components: a nanoscale double barrier quantum well (DBQW) resonant tunneling diode photodetector (RTD-PD)[42,43] in an optical ridge waveguide, and a laser diode (LD). Both components operate at telecommunication wavelengths ($\sim$1.55 μm). The typical electrical active area of the RTD-PDs used in our work is around 400 μm^2 and the ridge mesas of the commercial lasers have typical areas of $\sim$300 μm^2. Although the footprint of both devices is currently much larger than the nanoscale dimensions of the DBQW nanostructure (around 10 nm), our neuromorphic integrated system could potentially be reduced to dimensions (excluding the electrical contacts) of only a few micrometers taking advantage of recent advances in the nanofabrication of nanoscale light sources (nanoLEDs[44,45] and nanolasers[46]) with wavelength and sub-wavelength scale dimensions. Furthermore, RTD devices with areas below 25 μm^2 have been reported already by several groups, e.g., Refs. 47 and 48 although for different applications, namely, terahertz (THz) oscillators. This would bring several advantages since the energy per spike of the artificial neuron could be substantially reduced ($\ll$1 pJ) by scaling down both RTD-PD and LD components.

In the neuromorphic integrated system, the RTD-PD component provides a non-monotonic current-voltage (I–V) characteristic with a nonlinear region of negative differential conductance (NDC) (Fig. 2). Depending on the dc bias point, that is, the intersection point between the load line and the nonlinear I–V curve, the device can be operated in various dynamical regimes, in which the optoelectronic delayed feedback plays different roles:

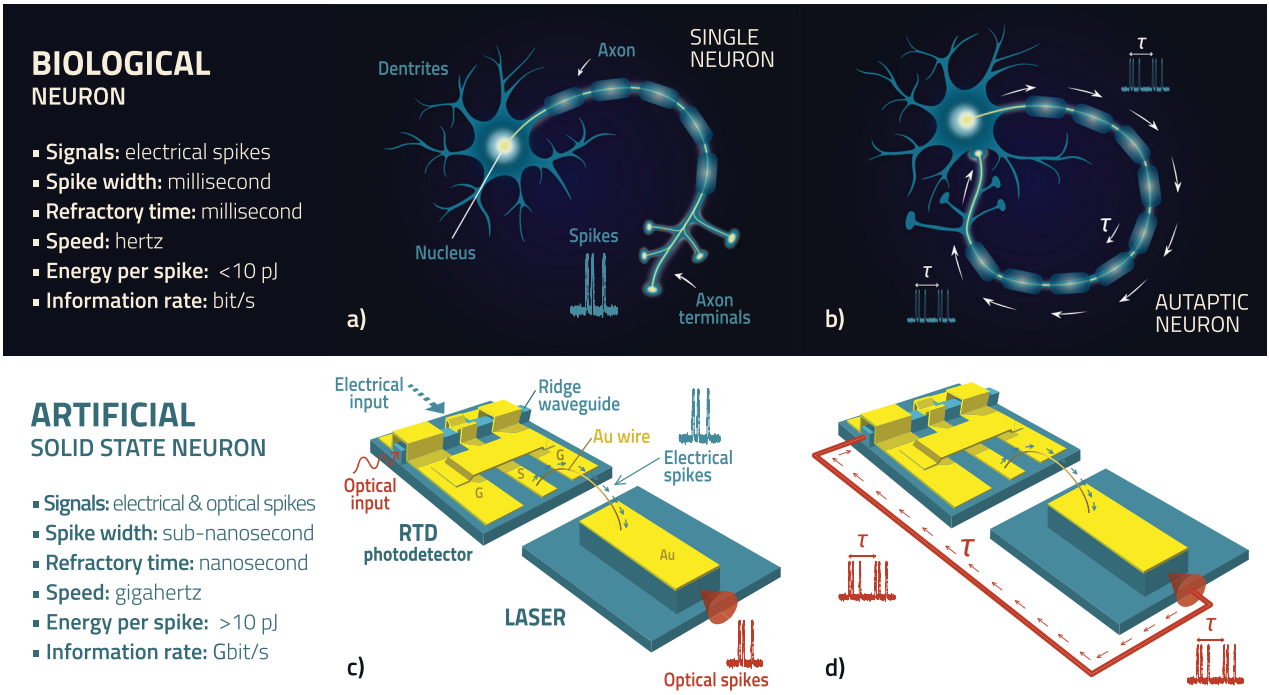

FIG. 1. (a) Artistic view of a biological neuron. (b) Representation of a neuron with a self-feedback connection with a time-delay τ due to the presence of an autapse. (c) The solid-state neuron microchip consisting of an RTD-photodetector connected in series with a semiconductor laser diode using a gold (Au) wire bond. Both electrical and optical high-speed excitable spike signals can be activated either electrically or optically. (d) Representation of the autaptic neuron microchip. In this configuration, the optical spiking output is re-injected into the RTD-photodetector input after a time-delay τ due to the propagation in an optical delay line (red trace). The typical performance of our artificial neuron and of a single biological neuron are both detailed in the bottom left and top left, respectively. The energy per spike was calculated using $E = \frac{1}{2}CV_{pp}^2$, assuming $C = 245$ pF and $V_{pp} = 100$ mV for the case of the biological neuron, while the electrical energy per spike of the artificial neuron assumed a typical device with $C = 4.5$ pF and $V_{pp} = 3$ V. The energy per spike of the artificial neuron can be substantially reduced ($\ll 1$ pJ) by scaling down the size of the microchip components.

1. **Bistability:** the load line can intersect the nonlinear *I–V* curve in one of its two positives slopes, also called positive differential conductance (PDC) regions (I and III in Fig. 2). Within either the two PDCs, the device remains at a steady-state but if the load line intersects both PDCs, bistability is achieved. In this bistable regime, the noise stemming from, e.g., thermal fluctuations in the circuit can induce transitions between the two stable states and a phenomenon of stochastic resonance is observed, as reported in Ref. 49.
2. **Self-sustained oscillations:** in the NDC, region II in Fig. 2, the system operates as a high-frequency nonlinear self-sustained oscillator.[50,66] In this situation, the quality of the high-speed radio-frequency signals can benefit from the high-quality factor of the delayed optoelectronic feedback,[51,52] enabling ultra-low phase noise self-sustained oscillations.
3. **Excitable dynamics:** when the bias point is set at the border between the first PDC and the NDC, region I in Fig. 2, neural, type II, excitable dynamics is achieved (see Sec. IV A for details on the physical principle of excitability). In the case of an asymmetric *I-V* curve, multi-pulse excitable bursting is obtained when biased at the border between the NDC and the second PDC, region III in Fig. 2. Depending on the perturbation and load line, periodic and aperiodic mixed mode oscillations can also be obtained under a proper external modulation (see Sec. IV B). In the excitable dynamic regime, the delayed optoelectronic feedback leads to self-regeneration of the fired excitable pulses enabling regenerative memory operation, as discussed in detail in Sec. IV C.
4. **Neural inhibition dynamics:** although not discussed in this review paper, our system could be used to obtain neural inhibition dynamics.[27,53] In this case, the bias point is set in the NDC and close to the peak, region II in Fig. 2, where oscillations are obtained. In order to get a static response, that is inhibition, an external voltage can be applied (using, e.g., a negative pulse voltage) to switch the operation point to the first PDC region, region I in Fig. 2. The same principle can be used in the case the bias point is set in the NDC region but closer to the valley. In this situation, a positive pulse voltage is needed to switch the operation point to the second PDC region, region III in Fig. 2.

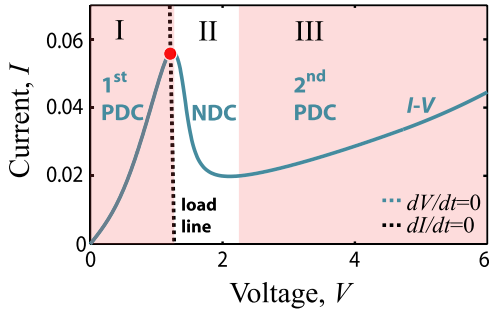

FIG. 2. Typical asymmetric nonlinear current-voltage characteristic (solid curve) of a resonant tunneling diode showing the regions of negative (II) and positive (I and III) differential conductance. Also shown is the load line (dashed curve) which defines the operating point of the RTD-based neuromorphic optoelectronic circuit.

In this review article, we address the neural spike dynamic characteristics detailed above in the excitable dynamic regime (point 3) combined with a mechanism of time-delayed feedback. This corresponds to the solid-state autaptic neuron configuration represented schematically in Fig. 1(d). It consists of an optical delay line inserted off-chip,[54] typically using a low loss optical fiber, with a time delay of τ. The delay line provides a mechanism of re-injection of the fired optical pulses, analogous to the autaptic neuron shown in Fig. 1(b). This scheme is exploited for applications in brain-inspired temporal buffer memories enabling writing and storage of information as light intensity pulses. Notably, the neural spike response in the autaptic configuration displays all the signatures of spatio-temporal localized structures (LSs) of light (see a recent review in Ref. 55) As discussed in Sec. IV E, by taking advantage of the dissipative nature of the LSs, robust and flexible data reconfiguration and clock and timing can be achieved in our neuromorphic chips at high-speeds and with short transients.

II. NANOSCALE RESONANT TUNNELING DIODE

The quantum properties of charge transport and the nonlinearity of nanoscale RTDs have been exploited in a large variety of applications including THz communications,[56] THz imaging,[57] ultrashort pulse generators,[58] highly sensitive light detectors,[43,59,60] single-photon detectors and photon counting,[61–63] ultrafast memories and switches,[64] and emulation of neural excitable responses.[41,49,54,65] Here, we give particular attention to the mechanism of charge transport based on quantum resonant tunneling that provides the N-shaped negative differential conductance in RTDs, a key property enabling excitable neural responses in nanoscale RTDs.

Figure 3(a) shows a schematic example of the energy diagram of a resonant tunneling diode formed by InGaAs/AlAs compound semiconductors. Its nanostructure consists of a low energy band-gap semiconductor with energy E_{gw}, typically a quantum well ranging from 5 nm to 10 nm wide, surrounded by two thinner layers of higher energy band-gap semiconductor barriers (with energy E_{gb}), typically ranging from 1.5 nm to 5 nm wide, both sandwiched between lower energy band-gap materials, usually the quantum well material. When both sides are terminated by highly doped semiconductor layers for electrical connection (the emitter and the collector contacts), the nanostructure is called a resonant tunneling diode. These types of low-dimensional nanostructures have attracted a large attention because of the pronounced region of NDC that appears in their I–V characteristics over a wide voltage range [Fig. 3(b)].

A. Double barrier quantum well nanostructure

The carrier flow through a double barrier quantum well resonant tunneling diode (DBQW-RTD) is fundamentally different from that of a single barrier because the DBQW structure acts as filter to charge carrier energy distribution by controlling the number of carriers that can take part in the conduction through the resonant levels. In the scheme of Fig. 4, it is shown a comparison between the transmission coefficient, $T(E)$ [panel (c)], for a single barrier, panel (a), and a symmetric double barrier quantum well, panel (b), as a function of the incident charge carrier energy, E. For the case of a symmetric double barrier, because of the finite height of the energy barriers, the allowed energy states in the well region become quasi-bound (or resonant states) rather than bound states. As a consequence, tunneling of charge carriers through the barriers is strongly enhanced (reaching unity), black line in Fig. 4(c), for incident energies that equal the nanostructure resonant energies. The transmission coefficients in the double barrier quantum well case are much higher than the transmission coefficients of a single barrier at the same energy values of the resonant levels; see green dashed-point trace in Fig. 4(c). The transmission coefficient lobs broaden with increasing energy because the barriers become more transparent. The carrier transmission coefficient maxima shown in Fig. 4(c) give rise to a current-voltage characteristic with regions of maximum and minimum conduction, resulting in an N-shaped

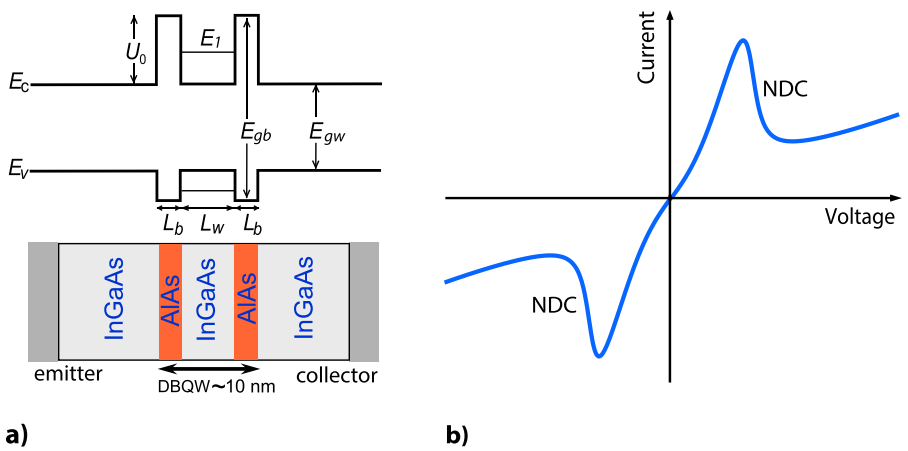

FIG. 3. (a) Schematic energy diagram (top) of the lowest conduction band, E_c, and the highest valence band, E_v, of a double barrier quantum well nanostructure formed by InGaAs/AlAs semiconductor compounds (bottom). E_{gb} and E_{gw} represent the energy bandgaps of the barriers and quantum well, respectively, and U_0 is the potential barrier height. (b) Typical antisymmetric N-shaped current-voltage characteristic of a DBQW-RTD nanostructure at room-temperature showing the regions of negative differential conductance. Reproduced with permission from Romeira, Ph.D. thesis (Universidade do Algarve, 2012). Copyright 2012 Bruno Romeira.

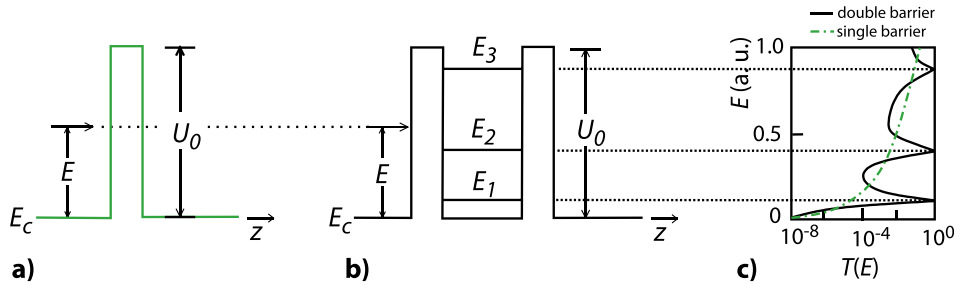

FIG. 4. Schematic diagram showing (a) a single barrier, (b) a symmetric double barrier quantum well nanostructure, and (c) the corresponding transmission coefficients, $T(E)$, as a function of incident carrier energy, E. U_0 is the potential barrier height, and $E_1 - E_3$ are the resonant energy levels. Reproduced with permission from Romeira, Ph.D. thesis (Universidade do Algarve, 2012). Copyright 2012 Bruno Romeira.

change of the current flow as a function of the applied voltage.

B. Negative differential conductance

The N-shaped RTD I–V characteristic can be understood with the help of the lowest conduction band profile. The top panels in Fig. 5 show the schematics of the lowest conduction band profiles for an n-type DBQW-RTD at zero volt, panel (a), at the peak voltage (resonance), panel (b), and at the valley voltage (off resonance), panel (c). When the applied bias is small, i.e., $V \ll V_p$ (where V_p is the peak voltage, also referred as resonance voltage), the conduction band profile is not much affected, remaining almost flat [see Fig. 5(a)]. The first resonant level is well above the emitter's Fermi level, and very low charge flows. As the voltage is increased, the energy of the first resonant level is moved downwards to the emitter's Fermi level, leading to an almost linear increase of the current with the voltage. The current increases until a local maximum is reached at I_p, ideally, at $V \simeq 2E_{n=1}/q$, that is, when the overlap between the emitter's Fermi sea energy and the transmission coefficient around the first resonant level reaches a local maximum, see Fig. 5(b) upper panel, corresponding to the first positive differential conductance region. A further increase in the applied voltage pulls the first resonant level towards the bottom and into the forbidden band-gap, where there are no longer carriers available to efficiently cross the DBQW. This leads to a sharp current decrease, giving rise to the first NDC portion of the I–V characteristic. At a given voltage, called the valley voltage V_v ($V_v > V_p$), the current reaches a local minimum I_v [Fig. 5(c)]. An additional increase of the bias voltage will further lift up the emitter's Fermi level and tunneling through higher resonant levels or carrier transport above the barriers will lead to a new current increase.

C. Liénard oscillator model

Using the theory of nonlinear differential equations employed to describe oscillator systems, here we formulate the nonlinear dynamic model that describes the dynamic characteristics of resonant tunneling diode resonators. The RTD is represented by an equivalent parallel circuit describing the RTD's conductance G_0 and its capacitance C as

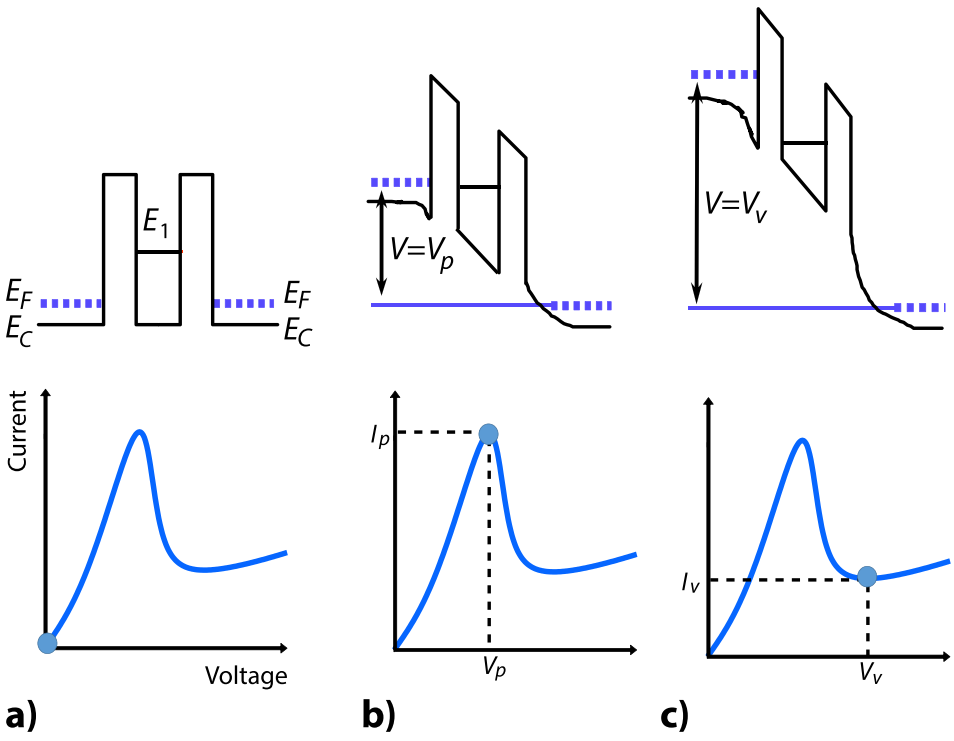

FIG. 5. (a)–(c) Lowest conduction band profile under applied voltage (top), and corresponding N-shaped negative differential conductance current-voltage characteristics (bottom). Reproduced with permission from Romeira, Ph.D. thesis (Universidade do Algarve, 2012). Copyright 2012 Bruno Romeira.

shown in Fig. 6. The RTD conductance and the diode capacitance correspond to the static NDC conductance and the RTD's emitter-collector capacitance, respectively. We use a voltage dependent current source, $I = F(V)$ to model the nonlinear I–V characteristic. The function $F(V)$ describes the experimental N-shaped I–V characteristic and can be either fitted with a polynomial function or using a more detailed equation.[67] Since the RTD current lags behind the applied voltage, an inductance in series with the RTD conductance should be considered in the circuit model. This inductance L_{qw} is related with the resonant state given by $L_{qw} = \tau_d/G_0$, where τ_d is the resonance lifetime. However, in a real circuit operating at moderate frequencies <10 GHz, L_{qw} is negligible, that is, much smaller that the circuit's inductance, Fig. 6.

By applying Kirchhoff's rules (using Faraday's law) to the circuit of Fig. 6, the voltage $V(t)$ across the capacitance C and the current $I(t)$ through the inductor L are given by the following system of two first-order differential equations:

$$\mu \frac{dV(t)}{dt} = I(t) - F(V) - I_n - I_{ph}, \tag{1}$$

$$\mu^{-1} \frac{dI(t)}{dt} = V_{dc} + V_{ac} \sin(\omega_{in} t) - RI(t) - V(t), \tag{2}$$

where V_{dc} is the dc bias voltage and L describes the circuit parasitics from the transmission line and wire connections. Lastly, R is the series resistance related to the highly doped bulk regions on either side of the DBQW structure and the external lead resistances associated to the contacts, e.g., wires and other bias circuit components. We also include in Eq. (1) an external electrical perturbation $V_{ac} \sin(2\pi f_{in} t)$ describing a sinusoidal modulation, where V_{ac} represents the amplitude and f_{in} its frequency. For purposes of numerical simulation time was rescaled by the RTD natural frequency $\omega_0 = 1/\sqrt{LC}$ so that $\mu = \sqrt{C/L}$, $f_{in} = \frac{\omega_{in}}{\omega_0 2\pi}$.

In Eqs. (1) and (2), when $V_{AC} = 0$, the system is called an autonomous Liénard oscillator.[68] The Liénard's model describes a wide range of physical nonlinear dynamical systems (see Refs. 68 and 69 and the references therein). More recently, we have demonstrated the Liénard system describes the rich dynamics of RTD optoelectronic oscillators, specifically the generation of self-sustained oscillations at GHz speeds.[50,52] The Liénard RTD oscillator subjected to a time-dependent external force ($V_{ac} \neq 0$) provides an additional degree of freedom and a wide range of additional dynamical regimes besides self-sustained oscillations can emerge.

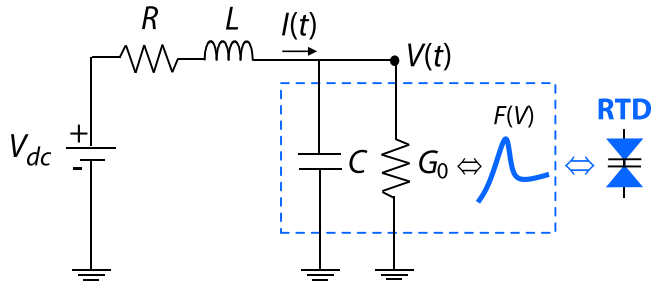

FIG. 6. Equivalent lumped electrical circuit schematic of the nanoscale RTD nonlinear oscillator. Reproduced with permission from Romeira, Ph.D. thesis (Universidade do Algarve, 2012). Copyright 2012 Bruno Romeira.

Foremost of these dynamical regimes include synchronization,[70,71] chaos,[72,73] and excitability.[41] Lastly, the photocurrent, I_{ph}, and current noise, I_n, sources included in Eq. (1) describe the Liénard oscillator under optical injection[42] and perturbed by current noise,[52] respectively. The photodetection characteristics of the RTD are analyzed in detail in Sec. III A.

III. SOLID-STATE OPTOELECTRONIC NEURON RESONATOR

In this section, we present our work on recently developed solid-state optoelectronic neuron microchips formed by resonant tunneling diode oscillators. In our approach, electronic and photonic components are hybrid integrated in a single chip enabling electro-optical neuromorphic functionalities. Figure 7 shows a schematic representation of the individual and hybrid integrated microchips, panels (a)–(c), and their respective equivalent circuits, panels (d)–(f) used to model the experimental circuits. In what follows, we describe, both experimentally and theoretically, the implemented optoelectronic circuits for neuromorphic applications.

A. RTD-photodetector

The key component of our solid-state neuron microchips is the RTD-photodetector [Fig. 7(a)]. It consists of a DBQW embedded in an optical ridge waveguide and operates as a waveguide photodetector for incoming light at wavelengths with energy close to or above the waveguide core bandgap energy (the typical operation of our devices is $\sim$1.55 μm). Its typical epi-layer structure is grown by molecular beam epitaxy in a Varian Gen II system on an InP substrate and consists of a 2-nm-thick AlAs barriers separated by a 6-nm-wide InGaAs layer, embedded in a 1 μm thick ridge waveguide which corresponds to the photoconductive semiconductor layers. The ridge waveguide consists of a unipolar InAlAs/$In_{0.53}Ga_{0.42}Al_{0.05}As$/InP (for more details, see Refs. 43 and 74). As represented schematically in Fig. 7(a), such configuration enables control of the neuron microchip using both light and electrical signals.

The dynamics of the RTD-PD is analyzed considering the lumped electrical circuit of Fig. 7(d). This circuit is equivalent to the Liénard oscillator circuit analyzed in Sec. II C, Fig. 6, but assuming an additional photocurrent, I_{ph}, and current noise, I_n, sources [already described in Eq. (1)]. The photocurrent source, I_{ph} (see below), describes the photogenerated current in response to an optical modulated signal. The current noise source, I_n, describes the random noise processes in the oscillator and detector, specifically thermal and shot noises, and are all modelled as Gaussian noise processes (and are described in Sec. III C).

In Eq. (1), the RTD-PD photo-generated current, I_{ph}, in response to an optical modulated signal, $P(\lambda)$, is given by

$$I_{ph} = \eta_{ph} \frac{e\lambda}{hc} P(\lambda), \tag{3}$$

where λ is the wavelength, e is the electric charge unit, h and c are the Planck constant and the speed of light in the

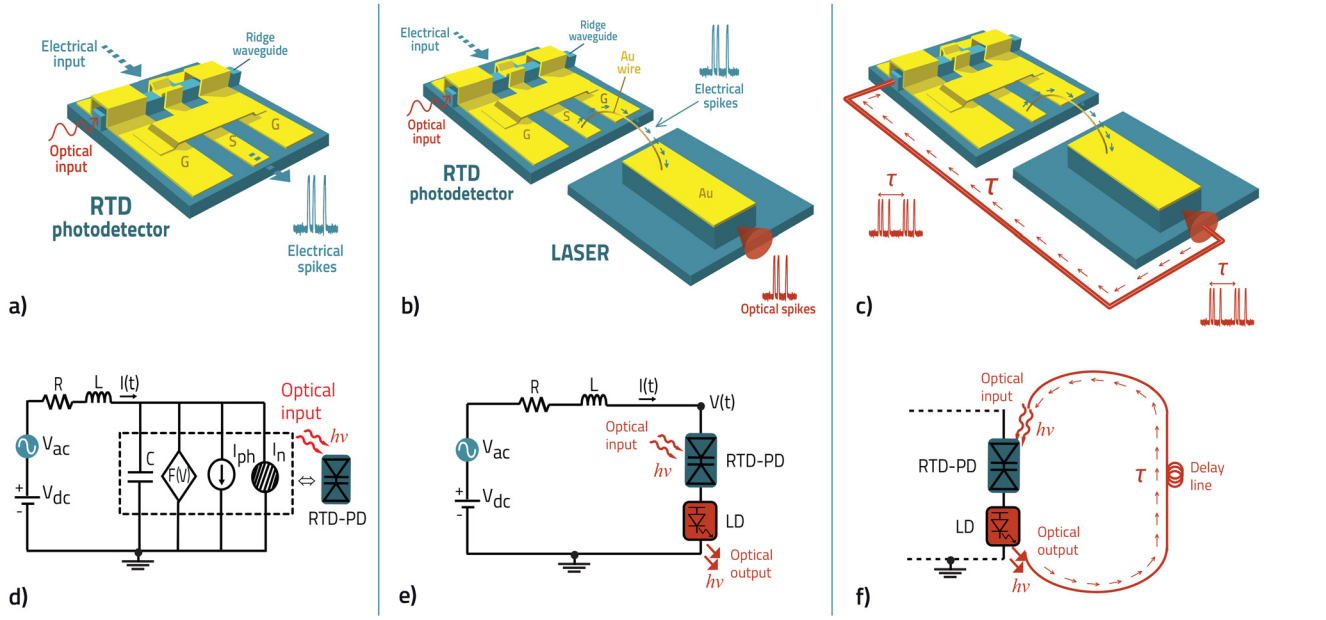

FIG. 7. (a) Schematic of the solid-state neuron microchip consisting of the RTD-photodetector (RTD-PD). (b) Schematic of the solid-state optoelectronic neuron microchip consisting of an RTD-PD connected in series with a semiconductor laser diode using a gold (Au) wire bond. Both electrical and optical high-speed excitable spike signals can be activated either electrically or optically. (c) Schematic of the autaptic neuron microchip. In this configuration, the optical spiking output is re-injected into the RTD-photodetector input after a time-delay τ due to the propagation in an optical delay line (red trace). Schematic representation of the equivalent lumped electrical circuits of (d) the RTD-PD microchip, (e) the RTD-PD-LD microchip, and (f) the autaptic microchip.

vacuum, respectively, and η_{ph} is the waveguide photodetector quantum efficiency given by

$$\eta_{ph} = \kappa(1 - R_{ref})(1 - e^{-\alpha\gamma_{ph}\Lambda}), \tag{4}$$

where κ is the light coupling factor, R_{ref} is the waveguide facet reflectivity, α is the waveguide core absorption coefficient, γ_{ph} is the overlap integral of the electric and the optical fields, and Λ is the active waveguide PD length. Typical values can be found in Ref. 43.

Although the I–V characteristic of the RTD-PD is a function of both voltage and optical power,[43] considering the low responsivity of the photodetectors analyzed (<0.25 A/W), in this work, we assume the static I–V curve in dark conditions. In the cases where the optical injection changes substantially the I–V characteristic, refinements of the model can be included, namely, by taking into account the photoconductivity and charge accumulation effects in double-barrier RTD structures (see, for example, the work of Ref. 75).

B. RTD-laser diode

In the RTD-laser diode configuration [Fig. 7(b)], the RTD-PD is connected in series with a laser diode in a hybrid optoelectronic integrated circuit, Fig. 7(e). The typical laser devices used in our work consisted of an InGaAsP multi-quantum-well active region operating in continuous-wave at ~1550 nm, with 6 mA threshold current, up to 10 mW optical output power, and a modulation bandwidth of ~10 GHz. Connecting a laser diode in series does not substantially change the overall shape of the nonlinear I–V characteristic of the RTD. As detailed in Ref. 50, it just shifts the peak and valley regions to higher voltages (a shift of around 0.84 V, i.e., the voltage drop across the laser p–n junction) while the current values are unchanged. In fact, the nonlinearity of the RTD-PD remains in the laser output. The RTD-PD provides a dynamical bias current control for the laser diode enabling the RTD-LD to operate as a neuromorphic optoelectronic oscillator featuring high-speed response and quadruple electronic and optical input/output functionalities. Moreover, this configuration can be readily adapted to include other types of laser devices (e.g., vertical-cavity surface-emitting lasers), and on-chip monolithic integration of both RTD-PD and LD components can also be implemented.[76]

In order to describe the dynamic behavior of the laser diode employed in our neuromorphic microchips, we use a single-mode rate-equation model. The rate equations for the photon, $s(t)$, and carrier, $n(t)$, densities in the semiconductor laser active region are given by

$$\frac{dn(t)}{dt} = \eta_i \frac{I(t)}{qV_a} - \frac{n(t)}{\tau_n} - g_0(n(t) - n_0)s(t), \tag{5}$$

$$\frac{ds(t)}{dt} = \Gamma g_0(n(t) - n_0)S(t) + \Gamma\beta_{sp}\frac{n(t)}{\tau_n} - \frac{s(t)}{\tau_p}, \tag{6}$$

$$P_{opt} = \frac{\eta_{ext}V_a s(t)hc}{\Gamma\tau_p\lambda_c}, \tag{7}$$

where $I(t)$ is the modulated current provided by the RTD-PD [given by Liénard's model, Eqs. (1) and (2)], plus the dc current, V_a is the volume of the active region, τ_n and τ_p are the carrier lifetime and the photon lifetime, respectively; the spontaneous emission factor, β_{sp}, is the fraction of the spontaneous emission that is coupled to the lasing mode; n_0 is the carrier density at transparency; g_0 is the differential gain which includes the effect of gain compression; Γ is the optical confinement factor; λ_c is the emission wavelength; η_{ext} is the external efficiency; and P_{opt} is the laser optical output power.

For simplicity of analysis, the nonradiative recombination processes were neglected in the rate equations model.

C. Autaptic neuron resonator

Here, we describe how to operate and model the neuromorphic optoelectronic microchip described previously as an autaptic neuron. In this configuration, Figs. 7(c) and 7(f), an optical delay line with time-delay τ is inserted off-chip (typically a low loss optical fiber) providing a mechanism of re-injection of the optical output, analogous to an autaptic biological neuron [Figs. 7(c) and 7(f)]. As detailed in Sec. IV, this scheme is explored for applications in brain-inspired temporal buffer memories enabling writing and storage of information as light intensity pulses. In order to fully model this neuromorphic optoelectronic resonator system, we consider the set of Eqs. (1) and (2) describing the RTD-photodetector and the rate-equation model (5)–(7) describing the laser diode in a delayed feedback configuration. We then obtain the following dimensionless coupled delay differential equations (DDE) system describing the dynamic characteristics of the solid-state autaptic neuron:

$$\mu\frac{dV(t)}{dt} = I(t) - F(V) - \chi\xi(t) - \eta S(t-\tau), \tag{8}$$

$$\mu^{-1}\frac{dI(t)}{dt} = V_{dc} + V_{ac}\sin(\omega_{in}t) - RI(t) - V(t), \tag{9}$$

$$\tau_n'\frac{dN(t)}{dt} = \frac{I(t)}{I_{th}} - N(t) - \frac{N(t)-\delta}{1-\delta}\frac{S(t)}{1+\epsilon S(t)}, \tag{10}$$

$$\tau_p'\frac{dS(t)}{dt} = \frac{N(t)-\delta}{1-\delta}\frac{S(t)}{1+\epsilon S(t)} - S(t) + \beta_{sp}N(t), \tag{11}$$

where $N(t)$ and $S(t)$ are the dimensionless carrier and photon densities, respectively. The variables were rescaled as $n(t) = N(t)N_{th}$ and $s(t) = S(t)S_0$, where $S_0 = \Gamma(\tau_p/\tau_n)N_{th}$ and $N_{th} = n_0 + (\Gamma g_0\tau_p)^{-1}$ is the threshold carrier density; time is normalized to the characteristic LC resonant tank frequency, $\omega_0 = (\sqrt{LC})^{-1}$, hence $\tau = \omega_0 t$. The parameter $\eta S(t-\tau_d)$ is the optical feedback, where η is the feedback strength and τ is the time delay with respect to the dimensionless time t. The feedback strength parameter, η, depends on RTD-PD's detection characteristics [Eq. (3)] and the fraction of the laser optical output power P_{opt} re-injected into the delayed feedback loop. The carrier density in the laser Eqs. (10) and (11) is normalized to threshold, and I_{th} is the dimensionless laser diode threshold current. The parameters τ_n' and τ_p' come from the time rescaling. Last, we model the stochastic processes of the neuromorphic system (e.g., thermal and shot noises) as an effective delta-correlated Gaussian white noise of zero mean $\chi\xi(t)$,[77] Eq. (8), where the parameter χ is the dimensionless variance of the distribution and denotes the noise strength. Typical parameters used in the numerical simulations can be found in Ref. 52.

IV. EXCITABLE AND DELAY DYNAMICS

In this section, we review our recent results on the excitable and delay dynamic characteristics of both single and autaptic (self-delayed) solid-state neurons including all-or-none spike response (Subsection IV A), mixed mode oscillations (Subsection IV B), and spike-based data encoding, storage, and signal regeneration (Subsection IV C). In Subsection IV D, we link our experimental implementation of the artificial neuron to the paradigm of neuronal activity, the FitzHugh-Nagumo (FHN) model with delayed feedback. In Subsection IV E, we analyze in more detail our autaptic neuron and disclose the existence of a unique temporal response characteristic of extended spatio-temporal localized structures. As thoroughly discussed in Subsection IV E, the ubiquitous physical properties of these localized structures, namely, mutual independence, as demonstrated by their uncorrelated random walk motion in the presence of noise, enables the implementation of robust and flexible regenerative photonic memories by addressing, creating, and destroying individual localized pulsed patterns of information.

A. Excitability

Excitability is a concept originally coined to describe the capacity of living organisms, e.g., nerves[78,79] or neurons to respond strongly to a weak external stimulus that overcomes a well defined threshold. If the system is perturbed from its rest state, it may relax back towards its steady state in two different ways. If the perturbation remains below a certain threshold, the relaxation is exponential. Above this threshold, the system has to perform a large orbit that involves the whole phase space topology before relaxing again towards the unique fixed point (the rest state). Such a relaxation consisting of two widely different transient regimes towards a unique attractor defines the so-called excitability phenomenon (typically with a pulsed shape). Notably, this unique pulse (or spike) response depends only on the characteristics of the excitable system at hand and not on the details of the stimulus. During its large excursion in phase space, the system cannot respond to another perturbation which defines the so-called lethargic time (or refractory time), T_l, as the temporal extent of the orbit. Well known in physiology, this refractory period corresponds physically to the large amount of energy released during the excitable response and may be understood as the time the system needs to recharge before being able to release another response. In neurons, this period of time occurs during the re-polarization and the hyperpolarization of the membrane potential.

The unique characteristics of the excitable response confer to the data transmission and processing systems based upon this mechanism a high degree of robustness due to their inherent capability of signal reshaping. In the spatial domain, a photosensitive Belousov-Zhabotinsky reaction was used to perform image processing,[80] enabling smoothing and Sobel filter edge detection. Recently, an optical torque wrench[81] was employed as a sensing technique based in the excitability and was capable of detecting single perturbation events. In the last two decades, there has been a quest for electro-optical semiconductor excitable systems capable of operating at speeds much faster than the typical slow speeds of neurons. In electronic systems, neuron-like semiconductors[82] have

been explored showing moderate operation speeds (20 kHz). In the context of high-speed optical communications, short optical pulses (0.73 ns) were obtained using a monolithic vertical cavity laser with an intracavity saturable absorber.[83] Other examples of generation of fast optical excitable pulses can be found in Ref. 84 showing excitability in a quantum dot semiconductor laser with optical injection, and in Ref. 85 where much faster refractory times were reported using a micropillar laser with saturable absorber.

In what follows, we summarize our results on the artificial solid-state neuron of Figs. 7(b) and 7(e), operating at room temperature and at a telecommunication wavelengths (∼1550 nm) enabling high-speed neural pulse response. Our optoelectronic circuit contains the key ingredients that fulfill the excitability paradigm and thus the inherent capabilities for being used in the framework of bio-inspired photonic data processing. Specifically, this includes a potential for monolithic integration, an intrinsic high-speed response, and quadruple electronic and optical inputs/outputs.

1. Spiking and bursting

In order to operate the neuromorphic microchip of Figs. 7(b) and 7(e) and as an excitable system, the optoelectronic circuit is externally activated using either light or electrical signals and dc biased in a monostable condition (below or above the NDC region), that is, in a unique fixed point of at one of the PDC regions. In these conditions, the circuit is highly sensitive to the external input (using either a pulsed, square or noise signals), emitting fixed-shape spikes (or bursts of spikes), depending on the dc bias point. By choosing a white noise perturbation as the input signal, coherence resonance (CR) phenomena can be activated,[12] i.e., a maximum of temporal regularity in the output for a finite noise level.

Figure 8(a) presents experimental results showing the occurrence of spiking and CR behavior in a neuromorphic circuit activated by electrical noise. For a very weak noise input level, the output maintains its steady (rest) state. For a given noise threshold perturbation, panels (i) and (ii), the circuit is perturbed from its rest state and spiking in both electrical and laser outputs is observed (V and S, respectively). The spikes appear random, and the interval between excitations varies substantially. We show in the inset a single pulse event in both the electrical and the optical outputs. The upward voltage pulse event shows a full width half maximum (FWHM) of around 13 ns, inset of panel (i). The LD intensity output follows the electrical current switching induced by the RTD with a sequence of downward pulses of identical shape and typical FWHM of ∼200 ns, inset of panel (ii). For a moderate noise level, panels (iii)–(iv), the firing of spikes is more regular and the interspike intervals (ISIs) do not differ much, providing an example of coherence resonance behavior. An analysis of the statistics of the interspike interval (ISI) of the fired spikes allows us to estimate the refractory time to be around 500 ns (±20 ns).

Interestingly, the asymmetric I–V characteristic of our neuromorphic circuit enables two different excitable regimes. As detailed previously, in the first PDC, the response consists in a single isolated peak. But in the second PDC, the temporal response is composed by a succession (or burst) of peaks well separated by the lethargic time. In Fig. 8(a), panels (v) and (vi), is shown multi-pulsing“ bursting” behavior when the circuit is dc biased in the second PDC region. As explained next in more detail, in this case, the optical pulses are fired in an upward direction since the laser follows the electrical current switching induced by the RTD-LD.

The above observations can be fully explained with the model of Eqs. (8)–(11) (see Ref. 2 for details on the

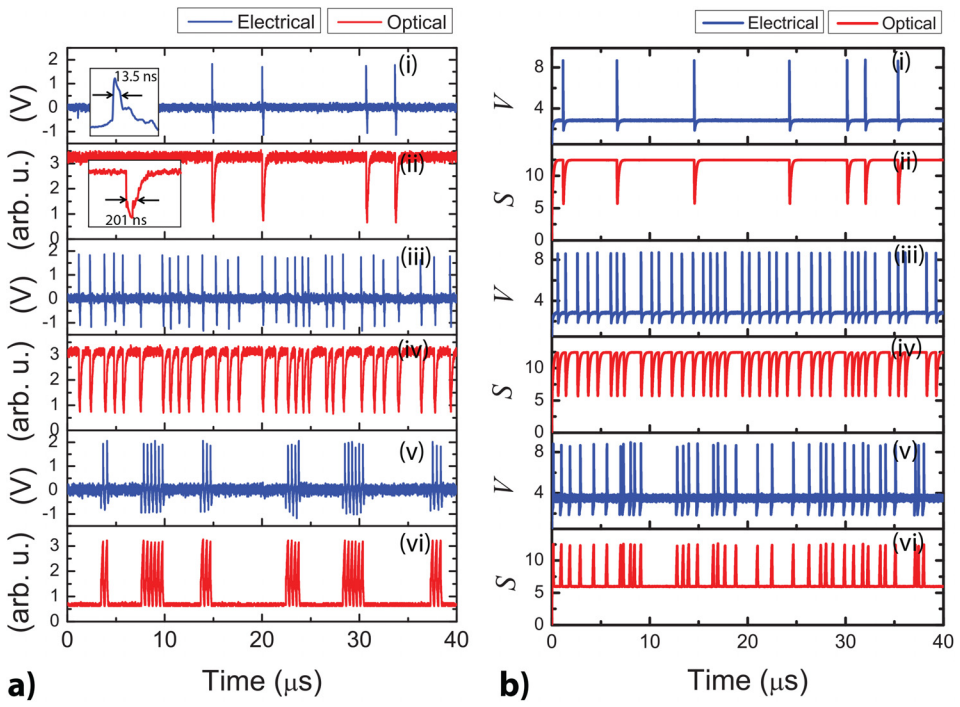

FIG. 8. (a) Experimental time traces of electrically noise induced neuron-like pulsing behavior in an RTD-LD excitable optoelectronic system in both the electrical and the optical domains. The RTD-LD is biased in the first PDC region and is modulated with a noise strength of (i)–(ii) 100 mV; (iii)–(iv) 175 mV. Multi-pulsing bursts when the RTD-LD is biased in the second PDC region and is modulated with a noise strength of 150 mV (v)–(vi). b) Numerical simulation of voltage and photon density (V, S) showing noise induced spike dynamic regimes (i)–(iv) in the first PDC, and (v)–(vi) in the second PDC. The dimensionless noise strength employed in the simulations are: (i)-(ii) $\chi = 0.128$; (iii)–(iv) $\chi = 0.158$; and (v)–(vi) $\chi = 0.310$. Reproduced with permission from Romeira *et al.*, Opt. Express **21**, 20931 (2013). Copyright 2013 Optical Society of America.

parameters used). Figure 8(b) shows a very good agreement between the numerical simulations and the experimental results in both electrical and optical outputs. The white Gaussian noise with amplitude above the excitable threshold activates randomly neuron-like pulses as observed experimentally. The multiple bursting in the second PDC is also predicted by the model due to the asymmetry of the $F(V)$ function.

The mechanism of pulse triggering is represented schematically in Fig. 9 and is explained as follows. The RTD-based autaptic neuron is an example of a slow-fast excitable system in which the fast variable is the voltage and the slow one the current. During the excitable orbit, the two fast stages correspond to a sudden increase and drop of the voltage during which the current does not changes appreciably. These two fast stages are interleaved by two slow stages in which the current evolves along the attracting nullcline as defined by the $F(V)$ function while the voltage follows adiabatically. In the limit $\mu \ll 1$, the two fast stages can be neglected and the lethargic time corresponds mainly to the evolution along the slow stages defined by the two PDC regions. In these regions, the motion is governed by the equation $dI/d(\mu t) = V_{dc} - RI - F^{-1}(I)$, that follows from the adiabatic elimination of V using that $\mu^{-1} \gg 1$. Since $F^{-1} \gg \gamma$, the period of the excitable orbit is proportional to $1/\mu = \sqrt{L/C}$ and to the derivative of F. Once the scaling of our model by $\omega_0 = (\sqrt{LC})^{-1}$ is removed, the lethargic time is solely proportional to the inductance of the circuit L. An approximate expression of the excitable period T_l can be estimated to be

$$T_l/L = \frac{1}{F_2^{-1}} \ln \frac{V_{dc} - F_2^{-1} I_+}{V_{dc} - F_2^{-1} I_-} + \frac{1}{F_1^{-1}} \ln \frac{V_{dc} - F_1^{-1} I_-}{V_{dc} - F_1^{-1} I_+}, \quad (12)$$

with $I_\pm$ the currents values at the folding points and $F_{1,2}^{-1}$ the inverse of the derivative of F in the first and second PDCs. The estimated inductance of the circuit analyzed in Fig. 8(a) was $L \sim 3$ μH, explaining the large measured lethargic time ($\sim$500 ns). As shown in the results of Subsection IV A 2, the lethargic time in our neuromorphic microchips can be substantially reduced using a transmission line with lower inductance to connect the RTD and the LD dies.

2. High-speed optically induced spike generation

Excitability and pulsating behavior can be achieved at much faster speeds as a result of modifications of our neuromorphic optoelectronic circuit. Using a transmission line with $L \sim 8$ nH to connect the RTD and the LD dies lethargic time can be substantially reduced. Figures 10(a) and 10(b) show downward and upward optical pulses, respectively, measured in the LD output and triggered by noise. In this case, excitation events were also triggered optically, panel (b), by coupling a light signal at 1550 nm to the RTD-PD ridge waveguide using a lensed optical fiber. The optical signal was amplitude modulated (AM) with electrical white noise. The RTD-PD shows a typical responsivity $\sim$0.2 A/W when dc biased in the second PDC region (see Sec. III A for more details concerning the RTD-PD). In the inset of Fig. 10(b), we show the single fired pulse events in both electrical and optical outputs. The optical pulse shows a FWHM of 5.4 ns, and the upward voltage pulse event shows a FWHM of around 0.46 ns. The measurements were limited by the time of sampling of the oscilloscope (100 ps).

Figures 10(c) and 10(d) present the corresponding ISI distribution. The ISI histogram analysis shows the time series measured in the first and second PDCs, showing the typical pulse statistics of the times between minima/maxima of the laser output computed using a bin size of 500 ps. We find a hard boundary on the left showing the typical exponential behavior of a Kramers escape process,[12] displaced by the refractory time of the excitable orbits. This analysis allow us to estimate a refractory time of 12 ns ($\pm$500 ps) in the first PDC region [Fig. 10(c)] and 9 ns ($\pm$500 ps) in the second PDC region [Fig. 10(d)]. The lethargic time is more than one order of magnitude lower than the lethargic time measured in the previous neuromorphic circuit analyzed ($\sim$500 ns). Further speed increasing and pulse width reduction is expected with future improvements of the microchips which include reducing the RTD-PD active area (and

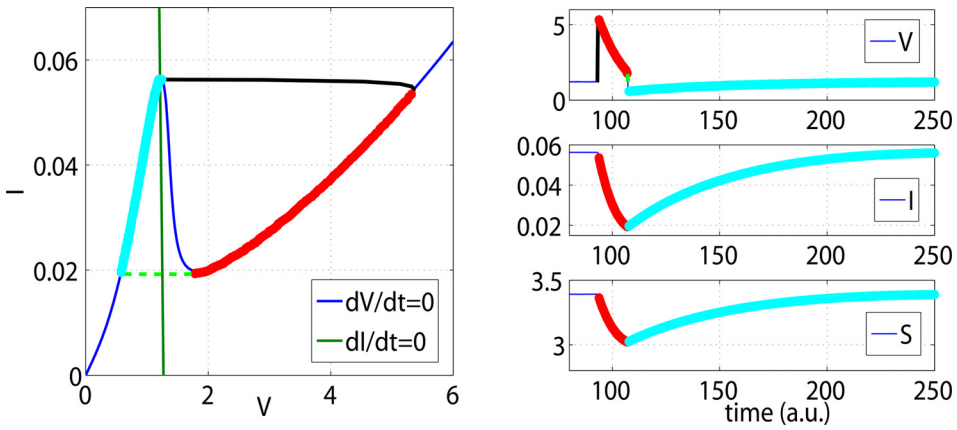

FIG. 9. Decomposition of the excitable orbit into four stages. The first fast stage corresponds to a sudden rise of the voltage (black line) without variation of the current. The second stage consists in a slow decay of both V and I along the right part of the $F(V)$ nullcline (red line). Next, another fast stage correspond to a voltage drop to the other side of the same nullcline (green dotted line) without variation of the current, finally followed by last slow stage where both V and I recover their initial values (light blue line). The laser output being modulated by the current, only the slow stages drive its dynamic evolution. Reproduced with permission from Romeira *et al.*, Opt. Express **21**, 20931 (2013). Copyright 2013 Optical Society of America.

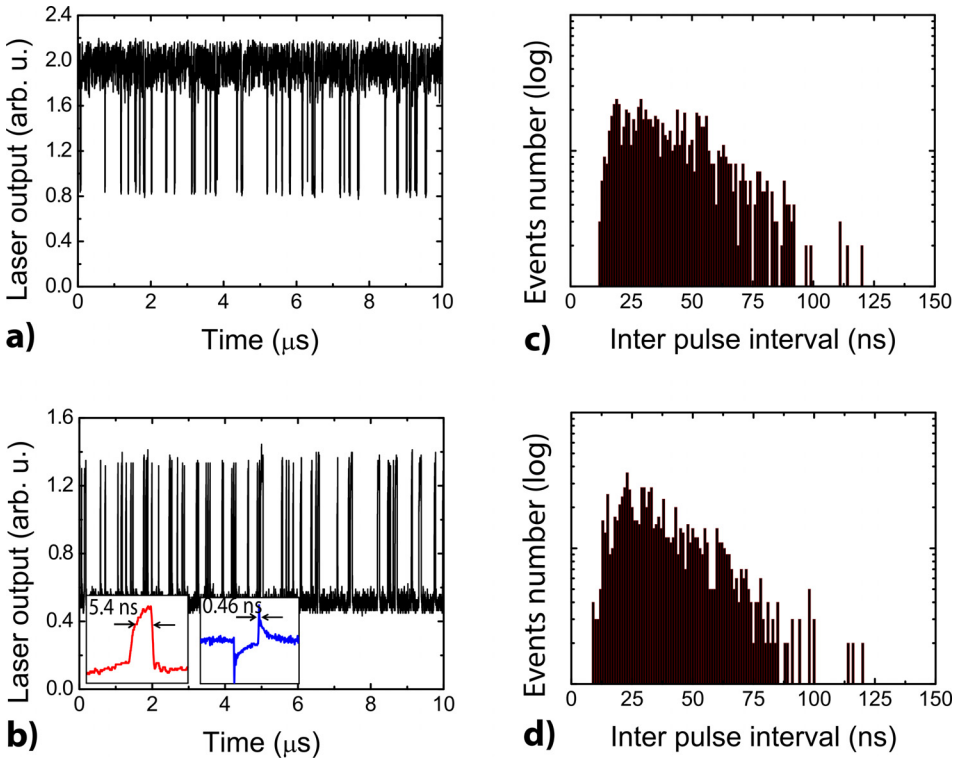

FIG. 10. Experimental time traces of the photo-detected laser optical output: (a) electrically noise induced pulsing in the first PDC using a noise amplitude level of 600 mV; (b) optically induced pulsing in the second PDC using an optical power signal of 5.5 mW at $\lambda = 1550$ nm and AM modulated with an electrical noise signal with 1.5 V amplitude. Inset: optical and electrical single pulses. Statistic of the times between minima/maxima in the laser output (histogram bin size of 500 ps) when the RTD-LD is biased: (c) in the first PDC region, and (d) in the second PDC region. Reproduced with permission from Romeira *et al.*, Opt. Express **21**, 20931 (2013). Copyright 2013 Optical Society of America.

therefore reduce the intrinsic capacitance < 1 pF), and reducing the series equivalent inductance, mainly determined by the length of the gold wires used in the electrical connections.

B. Mixed mode oscillations

Mixed mode oscillations (MMOs) describe trajectories that combine small-amplitude oscillations and large-amplitude oscillations of relaxation type, both recurring in an alternating manner, as compared with the self-sustained relaxation oscillations. Recently, there has been a lot of interest in MMOs that arise due to a generalized canard phenomenon (see Ref. 86 and references therein). Such MMOs arise in the context of slow-fast systems, similar to our RTD-based neuromorphic system. The small oscillations arise during the passage of the trajectories near a fold, due to the presence of a so-called folded singularity. The dynamics near the folded singularity is transient, yet recurrent: the trajectories return to the neighborhood of the folded singularity by way of a global return mechanism.

In order to understand the dynamics of the MMO pattern generation in the case of our neuromorphic optoelectronic resonator,[87] we discuss the current-voltage phase space diagram displayed in Fig. 11(a). For the chosen parameters, the load line intersects the I–V in the first PDC region (rest state), but sufficiently close to the NDC region where self-sustained relaxation oscillations can occur. By choosing a periodic sinusoidal modulation, when the driving amplitude is below a given level of V_{ac}, the dynamics is only perturbed around the fix point, as shown in the upper left corner of the phase-space diagram. This corresponds to the small amplitude oscillations (binary "0"). If we increase the driving amplitude above a threshold value, oscillations of large amplitude (binary "1") can occur, corresponding to a large excursion in the limit cycle. Using this mechanism, MMO patterns of large and small (L^S) amplitude oscillations in the electrical domain are achieved. A typical waveform is displayed in Fig. 11(b), showing a periodic $L^S \rightarrow 3^1$ MMO

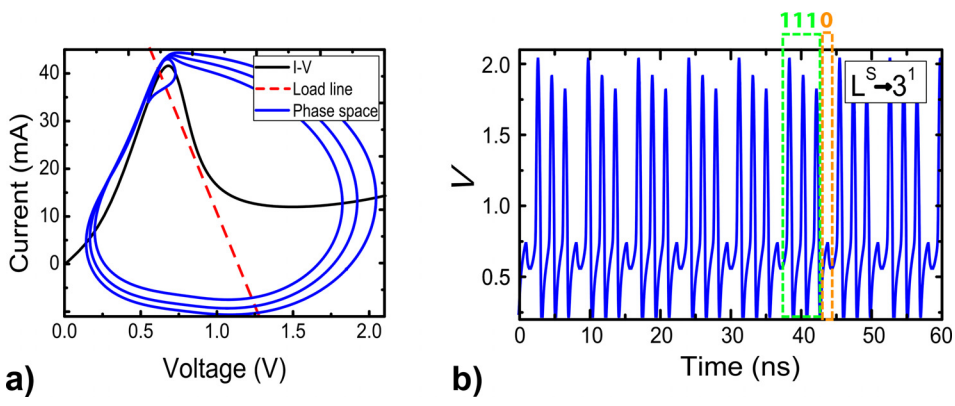

FIG. 11. (a) Nonlinear I–V curve, $F(V)$, load line, and numerically simulated limit cycle of a 3^1 MMO pattern. (b) A typical time series of a numerically simulated 3^1 MMO periodic pattern. Reproduced with permission from Romeira, Proceedings of the International Conference on Numerical Simulation of Optoelectronic Devices, NUSOD (2014). Copyright 2014 IEEE.

sequence with large amplitude signals of V followed by one small amplitude oscillation in the other state. The two-state level operation can be associated with a binary encoding {0, 1}. The L^S electrical current patterns directly modulate the laser diode, enabling identical MMO dynamics to occur in the LD intensity optical output.

In Fig. 12 is shown typical experimental time traces of MMOs patterns using a neuromorphic circuit similar to the one discussed in Sec. IV A 2. In this experiment, in order to operate the circuit as a two-state level MMO pattern generator, the bias point was selected in the second PDC region. Depending on the driving frequency and amplitude of the external control ac signal (assuming a fixed dc bias point and circuit parameters) either periodic or aperiodic intermittent MMO patterns can be triggered. In Fig. 12, we measured the response of the neuromorphic circuit to sinusoidal electrical signals in the range of 0.53 GHz to 0.63 GHz, that is, close to the natural oscillation frequency of the circuit, and recorded the laser photo-detected output using an oscilloscope. The results show that changing the periodic external signal will trigger an MMO sequence periodic of $L^S \rightarrow 3^1 \rightarrow 2^1 \rightarrow 1^1$, upon varying the frequency parameter. Between periodic MMOs, more complex patterns can be achieved including quasi-periodic and chaotic MMOs. In Fig. 12(d), we show an example of an aperiodic sequence displaying random MMOs.

The MMO pattern generation can be used as an efficient switching method to modulate the laser intensity output for applications in pattern and random bit generation. Considering that small external perturbations (in frequency or amplitude) substantially changes the dynamical characteristics of the MMO patterns, this can have novel applications in data encoding.

C. Regenerative photonic memories

Buffering of optical signals is desirable to avoid congestion of information traffic and realize efficient optical interconnects.

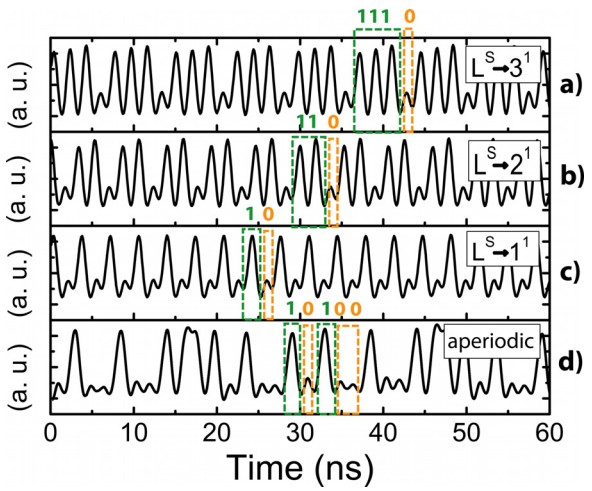

FIG. 12. Experimental time traces of periodic and aperiodic MMOs triggered by an external electrical periodic signal with an amplitude of 281 mV. The different MMO patterns are activated as a function of the injected frequency: (a) 0.544 GHz, (b) 0.564 GHz, (c) 0.586 GHz, and (d) 0.581 GHz. Reproduced with permission from Romeira, Proceedings of the International Conference on Numerical Simulation of Optoelectronic Devices, NUSOD (2014). Copyright 2014 IEEE.

Recently, all-optical buffer memories have been proposed based on slow-light delay lines, or using the Kerr nonlinearity on a standard silica optical fiber[88] providing functionalities such as all-optical storage and reshaping. However, for realistic applications, an optical buffer has to be compact for on-chip integration, which rules out most existing schemes, as they are not easily scalable to a millimeter size footprint and the writing process is often complex and costly. Therefore, configurations that combine the robustness of semiconductor nanoelectronic and optical devices with the wide-bandwidth of photonics elements offer significant advantages because they can provide small size, high-speed, and low cost alternatives to the all-optical buffers currently proposed.

In this section, we review our work on regenerative photonic memories using the autaptic configuration introduced in Figs. 6(c) and 6(f). In this configuration, an optical delay line with time delay τ is inserted off-chip (in this case, a low-loss single-mode optical fiber) providing a mechanism of re-injection of the fired excitable pulses analyzed in Sec. IV A, a mechanism analogous to an autaptic neuron. Our regenerative memory operates under the physical principle of excitable regeneration in which a pulse re-circulates indefinitely in an optical fiber delayed feedback loop enabling robust regenerative signal buffering and the potential for logical operations. The work on the solid-state autaptic neuron follows the strong interest that has been devoted during the past two decades on the effects of communication time delays in biological systems,[89,90] and how they can influence the synchronization dynamics between distant coupled neurons. For instance, it was shown that dynamical systems mimicking coupled neurons exhibit stable periodic pulsating regimes,[91–94] instead of a stable steady-state regime. Following the seminal work of Ikeda,[95] the concept of pattern memorization in time delayed bistable systems was addressed in opto-electronic systems, see for instance Refs. 96 and 97. Departing from these works, our work involves an excitable element, the RTD-PD resonator, as the nonlinear node. Because of this crucial difference, our approach benefits from the robustness and self-healing properties which are typical of neural signals and do not exist in bistable systems. Specifically, the excitable response of the nonlinear node guarantees a strong and well-defined all-or-nothing pulse response, almost identical in shape and duration to any supra-threshold incoming signal, enabling the reshaping and healing functionality of incoming signals which can be employed in the following critical telecommunication buffer functions: writing, storage, reshaping/healing, and XOR operation.

Figure 13 presents a typical example of experimental time traces showing the writing and storage of the regenerative memory using electrical injection of a single pulse bit, panel (a). The binary-coded data streams were generated using an arbitrary function generator. For purposes of demonstration and experimental convenience, the data signals were injected electrically although the signals could be also injected optically, taking advantage of the optical input port of the RTD-PD. By operating our solid-state autaptic neuron in an excitable regime (close to the NDC region), we are able to store and regenerate optical bits of information in the

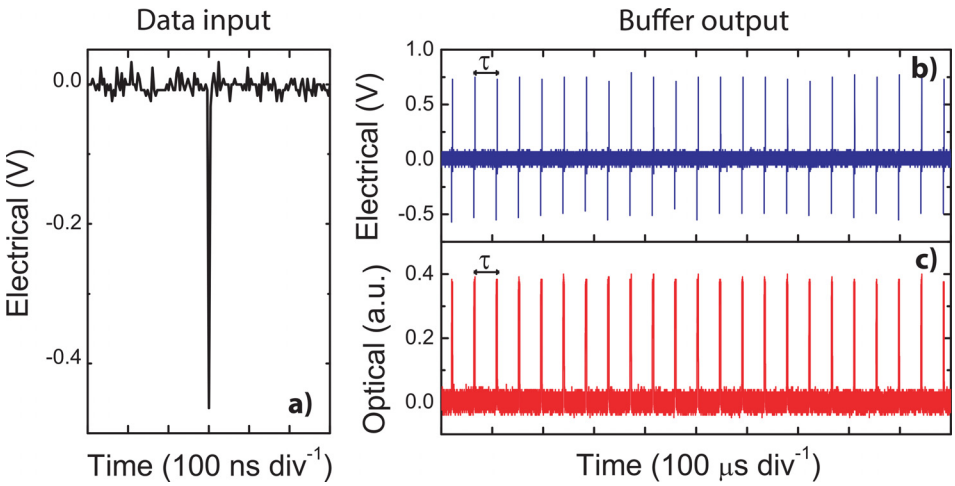

FIG. 13. Experimental recorded time traces of the regenerative memory output showing writing and storage of a single-bit electrical pulse in a $\tau = 46$ μs cavity round-trip time. (Left) single bit data input; (b) electrical and (c) laser photo-detected optical outputs.

fiber, the empty region signalling the "0" bits and the excitable optoelectronic pulses the "1." When these bits are re-injected into the RTD-PD, they trigger the generation of a new excitable cycle. This regenerative mechanism occurs after each round trip in the fiber which is extremely robust since even if the bit sequence is strongly deteriorated, the all-or-none nonlinear response of the excitable RTD-PD enables the signal regeneration. In the experiments, we used a low-loss optical fiber loop with a 46 μs cavity round-trip time, τ. The time τ was chosen in order that the memory buffer is much larger than the typical excitable lethargic time, T_l, of the RTD-PD-LD excitable system (in this case, $T_l \sim 500$ ns). In the results of Fig. 13(b) and 13(c), the regeneration lasted more than 10^4 time round-trips, only limited by the acquisition time of the oscilloscope employed. Real-time measurements suggest that storage of a data stream can be achieved for several minutes without using any temperature or vibration controllers of both optical fiber and optoelectronic circuits.

In order to assess the robustness of the writing and storage process, a wide range of temporal bit patterns were tested. Figure 14 shows an example of complete regeneration using two-bit (11), panel (a), and four-bit (1101), panel (b), patterns. The bits must be separated by the lethargic time T_l of the excitable system, which eventually defines the maximal bit rate as T_l^{-1}. The lethargic time induces a repulsion between nearest bits of data when they get too close, thereby ensuring signal integrity. Moreover, choosing a bit sequence where the amplitude of the bits are not evenly distributed, panel (c), the system is able to perform single pass healing by restoring and self-adjusting the received bits to a fixed amplitude. Thus, the unique characteristics of the excitable response of our neuromorphic system enables the implementation of novel types of regenerative memories almost insensitive (in a certain range) to the exact shape or amplitude of the incoming data signals. As presented in Fig. 15 showing complete regeneration using a more complex pattern of 8-bits (11011101), the writing and storage process of the regenerative memory is extremely robust. In this situation, the regeneration was stable within the ms range.

It is noteworthy that the writing process of the regenerative memory can be scalable to multi-gigahertz operation, only limited by the laser diode frequency response. The information can be written with a single addressing pulse, either using electrical or optical incoming data, and can be stored in standard low-loss single mode silica optical fibres, which is very beneficial for practical applications.

D. Time-delay FitzHugh-Nagumo model

A precise modeling of the experimental situation can be achieved within the framework of a dynamical model

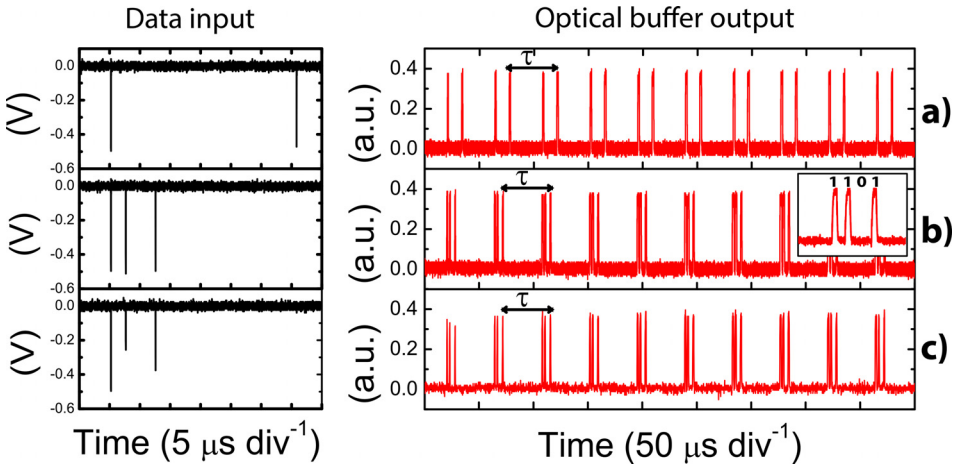

FIG. 14. Experimental recorded time traces of the regenerative memory output showing writing and storage of binary-coded data streams in a $\tau = 46$ μs cavity round-trip time. (Left) data streams input, and (right) laser photo-detected optical buffer output. Sequence of (a) 2-bit (11), (b) 4-bit (1101), and (c) and 4-bit (1101) binary-coded data streams.

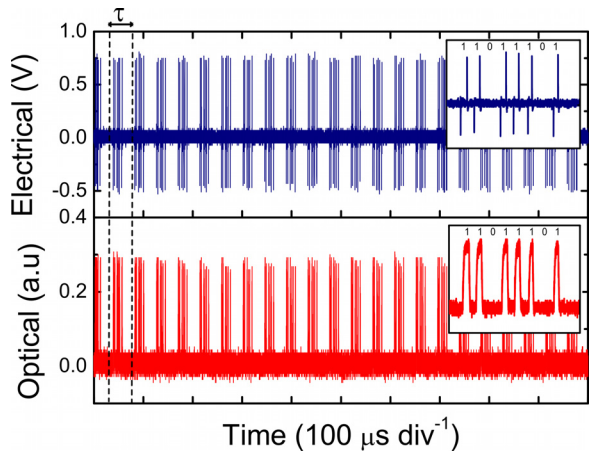

FIG. 15. Experimental recorded time traces of the regenerative memory showing storage of an 8-bit binary-coded data stream (11011101) in a $\tau = 46$ μs cavity round-trip time.

employing a Liénard equation. However, by assuming that the excitable response is slower than the relaxation oscillation frequency of the laser, one can adiabatically eliminate the laser intensity (S) that becomes slaved to the current (I) of the RTD. By expanding the nonlinear characteristic of the RTD at the center of the negative differential resistance, denoting δV and δI the deviation of the voltage and of the current, neglecting the asymmetry of the NDC region, i.e., we assume it is symmetric, one may reduce exactly the underlying physical model to the FitzHugh-Nagumo (FHN) model with delayed feedback, making a complete link with our time-delayed neuromorphic photonic system and the paradigm of excitability. The time delayed FHN model reads

$$\delta\dot{V} = \delta V - \frac{\delta V^3}{3} - \delta I + \eta[\delta I(t-\tau) - \delta I], \tag{13}$$

$$\delta\dot{I} = \varepsilon(\beta + \delta V). \tag{14}$$

The stiffness parameter $\varepsilon = \mu^2$ denotes the ratio of the time scale governing the slow and the fast variables while β is the effective bias parameter. We choose $\beta > 0$ without loss of generality. The influence of the delayed re-injection of light, proportional to the current in the RTD, is taken into account by the delayed term in Eq. (13). The amplitude of the delayed feedback is denoted η. For the sake of convenience we use the so-called form of noninvasive feedback.[98] As such, the steady states of the FHN model are unchanged by the presence of feedback. If not otherwise stated the parameters are $\varepsilon = 0.05$, $\eta = 0.18$, and $\tau = 500$. We included white Gaussian noise of variable amplitude ξ to model the stochastic processes occurring in our experimental neuromorphic photonic oscillator.

E. Spatio-temporal localized structures

The stored information in the optical delay line of the solid-state autaptic neuron is composed of coherent photon packets that possess all the properties of localized structures in delayed and spatially extended dynamical systems.[99] Localized structures have been widely observed in nature such as in granular media,[100] gas discharges,[101] reaction-diffusion systems,[102] fluids,[103] and convective systems.[104] Since the observation of LSs in semiconductor microcavities,[105] LSs analogues based in lasers have been exploited in periodically modulated and autonomous delayed dynamical systems[106–110] paving the way to novel methods of information storage, as proposed theoretically in Ref. 111.

We exemplify in Figs. 16(a)–16(d) various occurrences of such periodic regimes whose period are close to τ and that are composed of 0, 1, 3, and 6 bits of information as embedded excitable responses within the time delay τ. We stress in Fig. 16(e) that all these regimes coexist between themselves for a wide range of the bias parameter β. Because these isolated temporal patterns are bistable with the uniform state and are also independent of the boundary conditions, i.e., the time delay value, and are attractors of the dynamics, they can be considered as the equivalent of Localized Structures in time delayed systems.

Interestingly, each branch of solution corresponds to a well defined number of temporal LSs. However, what is hidden in such a projection is that for a given number of bits, i.e., a given branch, an infinity of different arrangements and relative distances exists. The storage capacity of our regenerative memory can be understood intuitively. Since the temporal extension of the excitable orbit is defined by its lethargic time T_l, the maximal amount of elements that can be stored in the time delay is the integer closest to $N \sim \tau/T_l$.

The full bifurcation diagram of the multi-LSs solutions was obtained with DDE-BIFTOOL[112] and is depicted in Fig. 17(b). The continuation of such solutions proved to be particularly challenging numerically and we were only able to study the equidistant multi-LSs solutions; see Ref. 54 for

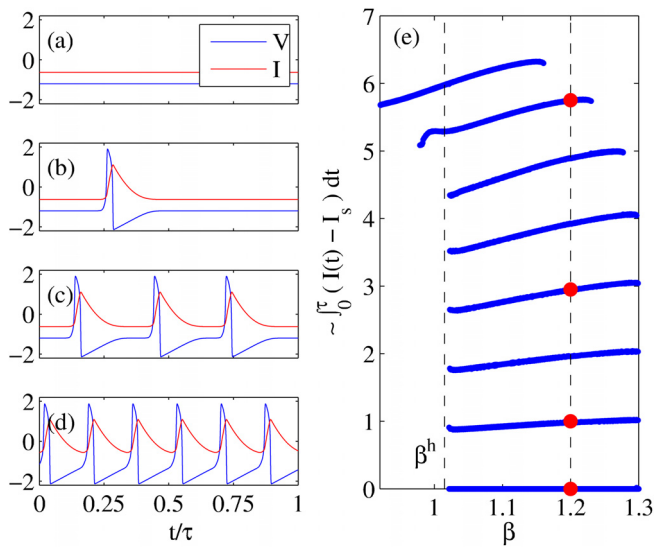

FIG. 16. Temporal time traces over a single period for various states of the regenerative memory (a)–(d) and multi-stability diagram of the coexisting solutions (e). In (e), we represent some norm of the solutions as the integral over one period of the deviation of the slow variable $(I - I_s)$ yielding upward pulses with a zero background. This integral is normalized to a value of 1 when there is a single pulse at $\beta = 1.3$. All the localized solutions become unstable close to $\beta^h \sim 1.018$ where the background get destabilized trough an Andronov-Hopf bifurcation. Reproduced with permission from Romeira *et al.*, Sci. Rep. **6**, 19510 (2016). Licensed under CC BY.

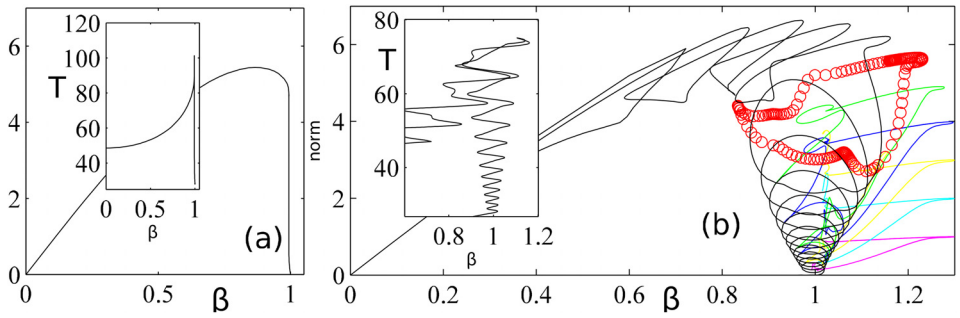

FIG. 17. Bifurcation theoretical analysis of formation of multiple states of memory. Left: Amplitude of the periodic solutions and variation of the period along the branches (inset) for the FHN system without feedback i.e., $\eta = 0$. Right: Same diagram with $\eta = 0.18$. The colors correspond to the branches of solutions with 1,2,…7, equi-spaced localized structures. Reproduced with permission from Romeira *et al*., Sci. Rep. **6**, 19510 (2016). Licensed under CC BY.

more details. We notice first that the simple bifurcation scenario found without feedback in Fig. 17(a) changes dramatically with $\eta \neq 0$. The dominant periodic branch that corresponds to the canard blow-up (in black) develops a large number of folds as apparent in Fig. 17(b). We stress that only the upper part of this folded branch is stable and that at, e.g., at $\beta = 1.1$, it corresponds to the solution with a maximal number of LS within the time delay, i.e., the trace depicted in Fig. 16(d) with $N = 7$. By analogy with the terminology of spatially extended systems we denote this particular temporal trace without empty regions as the fully developed pattern. We stress that in this regime, all the $N = 7$ pulses are interacting via their tails and can hardly be considered as independent. For instance, erasing an individual pulse would result in a smooth rearrangement of the other $N = 6$ remaining LSs in order to minimize their residual repulsive interactions. The other branches represented in colors in Fig. 17(b) correspond to solution with $N \in [1, 6]$ LSs. We refer the reader to Ref. 54 for the details regarding this analysis.

As another proof of the mutual independence of the temporal LSs, one can study their relative motion in presence of noise. For that purpose, we use a two dimensional pseudo-spatial representation in which the relative motion of the various LSs are best observed, Fig. 18. In this co-moving reference frame, the horizontal axis is a space-like coordinate that allows to localize the position of the pulses within a given round-trip while the vertical coordinate corresponds to the slow temporal evolution of the system over many round-trips; see Ref. 54 for details. The mutual independence of these pulses is demonstrated for instance by their uncorrelated random motion in the presence of noise. We also show the nucleation and annihilation process in Fig. 18(c) simply by including an extremely large amount of noise. One also notice here a property of the utmost importance: the almost total absence of transients: the localized bits of information can be perfectly written and erased in a single round-trip, in contrast with e.g., the results of Refs. 88, 107, and 113 where transients representing tens of round-trip are necessary before a stabilization of the waveform. From an application point of view, our time-delayed neuromorphic photonic memory presents the extraordinary advantage of enabling writing and erasing information at a rate comparable to the nominal reading rate.

V. PERSPECTIVES AND APPLICATIONS

The growing of artificial intelligence and the recognition by the semiconductor industry that the Moore's law is near its end is signaling a clear urgency for disruptive scientific concepts and technologies to keep up with the demands of low energy consumption and ultrafast computing and communications systems. Neuromorphic technologies combined with optics offer great promise for implementing compact, low power consumption artificial brain-inspired computing systems with real-time learning abilities.

Here, we have reviewed our recent work covering photonic memory circuits inspired by the biophysics of biological neurons. They consist of an integrated high-speed nanoscale nonlinear resonator and photo-detector, the resonant tunneling diode photo-detector (RTD-PD), a laser diode (LD), and an optical fiber, all operating at telecommunication wavelengths (∼1550 nm). This optoelectronic configuration forms a new type of high-speed nonlinear neuromorphic photonic resonator microchip, which emulates the biophysics of real spiking neurons and dynamic synapses.

The neuron-inspired photonic memory was demonstrated by sending a sequence of random bits of information

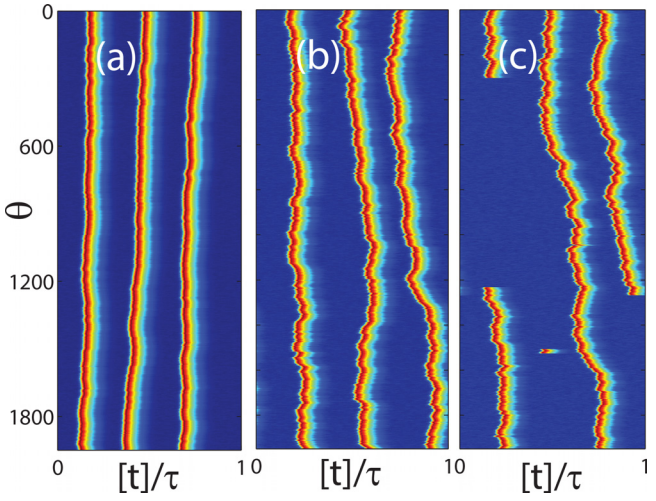

FIG. 18. The space-time plots represent the evolution of three LSs for an increasing level of noise. The slow variable represented is δI. In panel (a), $\xi = 10^{-3}$ and the noise induced drift motion is barely visible over more than $\theta = 2000$ periods. In panel (b), the uncorrelated random walk is more visible since $\xi = 5 \times 10^{-3}$ while in (c) the huge level of noise $\xi = 8 \times 10^{-3}$ is capable of inducing annihilation and nucleation of the LS.

that triggered the RTD-PD electro-optical spiking excitable response. Excitability is a nonlinear mechanism that not only governs the connections between neurons but also commands the rhythmic action of cardiac cells. Then, by delaying the excitable response using an optical fiber loop before re-injecting back into the RTD-PD input, we have demonstrated a regenerative memory as a result of the time-delayed feedback of the spiking nonlinear response of the system onto itself.

The impacts of this work are twofold. First, in our experiments, we were able to write, reshape, and store photon packets of information using conventional optical fibers at speeds much faster than the typical responses of biological neurons. The results are very promising for the development of disruptive brain-inspired high bit-rate (Gb/s) optical communications systems. Second, we have demonstrated that the stored information in the optical fiber is composed of coherent photon packets that possess all the properties of localized structures. Such states are abundant in nature and can be found in systems like granular media, semiconductors, fluids, and optical cavities. Their ubiquitous physical properties, namely, mutual independence, as demonstrated by their uncorrelated random walk motion in the presence of noise, enables a robust and flexible memory operation by easily addressing, creating, and destroying individual localized pulsed patterns of information.

Exploiting such a peculiar neuron-inspired response using photonics is a conceptual breakthrough that has been almost unexplored in the field of optical data communications and could open up new applications, e.g., clock and timing, optical memories and data buffers.

ACKNOWLEDGMENTS

This work was partially supported by the Fundação para a Ciência e a Tecnologia (FCT) under the Project UID/Multi/00631/2013, by the European Structural and Investment Funds (FEEI) through the Competitiveness and Internationalization Operational Program - COMPETE 2020 and by National Funds through FCT under the Project ALG-01-0145-FEDER-016432/POCI-01-0145-FEDER-016432, and by the European Commission under the project iBROW (Grant Agreement No. 645369). J.J. acknowledges financial support project COMBINA (TEC2015-65212-C3-3-PAEI/FEDER UE) and the Ramón y Cajal fellowship. We thank Charles Ironside, Curtin University, for the fruitful discussions on RTD optoelectronic devices, Oreste Piro, Universitat de les Illes Balears, for the useful discussions on excitable systems, and Raquel Luís for the artistic representation of the neuron.

[1]J. S. R. Jang, "ANFIS: adaptive-network-based fuzzy inference system," IEEE Trans. Syst., Man, Cybern. **23**, 665–685 (1993).
[2]H. A. Rowley, S. Baluja, and T. Kanade, "Neural network-based face detection," IEEE Transactions on Pattern Analysis and Machine Intelligence **20**(1), 23–38 (1998).
[3]G.-B. Huang, Q.-Y. Zhu, and C.-K. Siew, "Extreme learning machine: Theory and applications," Neurocomputing **70**, 489–501 (2006).
[4]P. Lichtsteiner, C. Posch, and T. Delbruck, "A 128× 128 120 dB 15 μs Latency Asynchronous Temporal Contrast Vision Sensor," in IEEE Journal of Solid-State Circuits **43**(2), 566–576 (2008).
[5]Y. Shen, N. Harris, S. Skirlo, M. Prabhu, T. Baehr-Jones, M. Hochberg, X. Sun, S. Zhao, H. Larochelle, D. Englund, and M. Soljacic, "Deep learning with coherent nanophotonic circuits," Nat. Photonics **11**, 441–446 (2017).
[6]G. E. Hinton and R. R. Salakhutdinov, "Reducing the dimensionality of data with neural networks," Science **313**, 504–507 (2006).
[7]Y. LeCun, Y. Bengio, and G. Hinton, "Deep learning," Nature **521**, 436–444 (2015).
[8]Y. Bengio, A. Courville, and P. Vincent, "Representation Learning: A Review and New Perspectives," IEEE Transactions on Pattern Analysis and Machine Intelligence **35**(8), 1798–1828 (2013).
[9]G. Indiveri, B. Linares-Barranco, T. Hamilton, A. van Schaik, R. Etienne-Cummings, T. Delbruck, S.-C. Liu, P. Dudek, P. Häfliger, S. Renaud, J. Schemmel, G. Cauwenberghs, J. Arthur, K. Hynna, F. Folowosele, S. Saïghi, T. Serrano-Gotarredona, J. Wijekoon, Y. Wang, and K. Boahen, "Neuromorphic silicon neuron circuits," Front. Neurosci. **5**, 73 (2011).
[10]P. A. Merolla, J. V. Arthur, R. Alvarez-Icaza, A. S. Cassidy, J. Sawada, F. Akopyan, B. L. Jackson, N. Imam, C. Guo, Y. Nakamura, B. Brezzo, I. Vo, S. K. Esser, R. Appuswamy, B. Taba, A. Amir, M. D. Flickner, W. P. Risk, R. Manohar, and D. S. Modha, "A million spiking-neuron integrated circuit with a scalable communication network and interface," Science **345**, 668–673 (2014).
[11]M. Prezioso, F. Merrikh-Bayat, B. D. Hoskins, G. C. Adam, K. K. Likharev, and D. B. Strukov, "Training and operation of an integrated neuromorphic network based on metal-oxide memristors," Nature **521**, 61–64 (2015).
[12]B. Lindner, J. Garca-Ojalvo, A. Neiman, and L. Schimansky-Geier, "Effects of noise in excitable systems," Phys. Rep. **392**, 321–424 (2004).
[13]See http://www.artificialbrains.com/darpa-synapse-program for SyNAPSE.
[14]B. V. Benjamin *et al.*, "Neurogrid: A Mixed-Analog-Digital Multichip System for Large-Scale Neural Simulations," Proceedings of the IEEE **102**(5), 699–716 (2014).
[15]See http://facets.kip.uni-heidelberg.de/ for FACETS.
[16]See https://www.humanbrainproject.eu/ for The Human Brain Project.
[17]See http://www.artificialbrains.com/spinnaker for SpiNNaker.
[18]See https://brainscales.kip.uni-heidelberg.de/index.html for BrainScaleS.
[19]G. Indiveri, E. Chicca, and R. Douglas, "A VLSI array of low-power spiking neurons and bistable synapses with spike-timing dependent plasticity," IEEE Transactions on Neural Networks **17**(1), 211–221 (2006).
[20]S. H. Jo, T. Chang, I. Ebong, B. B. Bhadviya, P. Mazumder, and W. Lu, "Nanoscale memristor device as synapse in neuromorphic systems," Nano Lett. **10**, 1297–1301 (2010).
[21]K.-H. Kim, S. Gaba, D. Wheeler, J. M. Cruz-Albrecht, T. Hussain, N. Srinivasa, and W. Lu, "A functional hybrid memristor crossbar-array/CMOS system for data storage and neuromorphic applications," Nano Lett. **12**, 389–395 (2012).
[22]D. Kuzum, S. Yu, and H.-S. P. Wong, "Synaptic electronics: Materials, devices and applications," Nanotechnology **24**, 382001 (2013).
[23]P. R. Prucnal, B. J. Shastri, T. F. de Lima, M. A. Nahmias, and A. N. Tait, "Recent progress in semiconductor excitable lasers for photonic spike processing," Adv. Opt. Photonics **8**, 228–299 (2016).
[24]B. Romeira, F. Kong, W. Li, J. M. L. Figueiredo, J. Javaloyes, and J. Yao, "Broadband chaotic signals and breather oscillations in an optoelectronic oscillator incorporating a microwave photonic filter," J. Lightwave Technol. **32**, 3933–3942 (2014).
[25]B. Romeira, F. Kong, J. M. L. Figueiredo, J. Javaloyes, and J. Yao, "High-speed spiking and bursting oscillations in a long-delayed broadband optoelectronic oscillator," J. Lightwave Technol. **33**, 503–510 (2015).
[26]P. R. Prucnal and B. J. Shastri, *Neuromorphic Photonics* (CRC Press/Taylor and Francis Group, Boca Raton, Florida, 2017).
[27]J. Robertson, T. Deng, J. Javaloyes, and A. Hurtado, "Controlled inhibition of spiking dynamics in vcsels for neuromorphic photonics: Theory and experiments," Opt. Lett. **42**, 1560–1563 (2017).
[28]H. V. D. Loos and E. M. Glaser, "Autapses in neocortex cerebri: Synapses between a pyramidal cell's axon and its own dendrites," Brain Res. **48**, 355–360 (1972).
[29]M. H. Flight, "Neuromodulation: Exerting self-control for persistence," Nat. Rev. Neurosci. **10**, 316 (2009).
[30]G. Tamás, E. H. Buhl, and P. Somogyi, "Massive autaptic self-innervation of GABAergic neurons in cat visual cortex," J. Neurosci. **17**, 6352–6364 (1997), http://www.jneurosci.org/content/17/16/6352.
[31]A. Bacci, J. R. Huguenard, and D. A. Prince, "Functional autaptic neurotransmission in fast-spiking interneurons: A novel form of feedback inhibition in the neocortex," J. Neurosci. **23**, 859–866 (2003), http://www.jneurosci.org/content/23/3/859.

[32]C. S. Herrmann and A. Klaus, "Autapse turns neuron into oscillator," Int. J. Bifurcation Chaos **14**, 623–633 (2004).
[33]L. Wiles, S. Gu, F. Pasqualetti, B. Parvesse, D. Gabrieli, D. S. Bassett, and D. F. Meaney, "Autaptic connections shift network excitability and bursting," Sci. Rep. **7**, 44006 (2017).
[34]Y. Xu, H. Ying, Y. Jia, J. Ma, and T. Hayat, "Autaptic regulation of electrical activities in neuron under electromagnetic induction," Sci. Rep. **7**, 43452 (2017).
[35]C. G. Rusin, S. E. Johnson, J. Kapur, and J. L. Hudson, "Engineering the synchronization of neuron action potentials using global time-delayed feedback stimulation," Phys. Rev. E **84**, 66202 (2011).
[36]M. Hashemi, A. Valizadeh, and Y. Azizi, "Effect of duration of synaptic activity on spike rate of a Hodgkin-Huxley neuron with delayed feedback," Phys. Rev. E **85**, 21917 (2012).
[37]H. Wang, J. Ma, Y. Chen, and Y. Chen, "Effect of an autapse on the firing pattern transition in a bursting neuron," Commun. Nonlinear Sci. Numer. Simul. **19**, 3242–3254 (2014).
[38]H. Wang, L. Wang, Y. Chen, and Y. Chen, "Effect of autaptic activity on the response of a Hodgkin-Huxley neuron," Chaos **24**, 33122 (2014).
[39]L. Appeltant, M. C. Soriano, G. Van der Sande, J. Danckaert, S. Massar, J. Dambre, B. Schrauwen, C. R. Mirasso, and I. Fischer, "Information processing using a single dynamical node as complex system," Nat. Commun. **2**, 468 (2011).
[40]I. Sourikopoulos, S. Hedayat, C. Loyez, F. Danneville, V. Hoel, E. Mercier, and A. Cappy, "A 4-fJ/spike artificial neuron in 65 nm CMOS technology," Front. Neurosci. **11**, 123 (2017).
[41]B. Romeira, J. Javaloyes, C. N. Ironside, J. M. L. Figueiredo, S. Balle, and O. Piro, "Excitability and optical pulse generation in semiconductor lasers driven by resonant tunneling diode photo-detectors," Opt. Express **21**, 20931 (2013).
[42]B. Romeira, J. M. L. Figueiredo, C. N. Ironside, A. E. Kelly, and T. J. Slight, "Optical control of a resonant tunneling diode microwave-photonic oscillator," IEEE Photonics Technol. Lett. **22**, 1610–1612 (2010).
[43]B. Romeira, L. Pessoa, H. Salgado, C. Ironside, and J. Figueiredo, "Photo-detectors integrated with resonant tunneling diodes," Sensors **13**, 9464–9482 (2013).
[44]K. C. Y. Huang, M. K. Seo, T. Sarmiento, Y. Huo, J. S. Harris, and M. L. Brongersma, "Electrically driven subwavelength optical nanocircuits," Nat. Photonics **8**, 244–249 (2014).
[45]V. Dolores-Calzadilla, B. Romeira, F. Pagliano, S. Birindelli, A. Higuera-Rodriguez, P. J. van Veldhoven, M. K. Smit, A. Fiore, and D. Heiss, "Waveguide-coupled nanopillar metal-cavity light-emitting diodes on silicon," Nat. Commun. **8**, 14323 (2017).
[46]M. T. Hill and M. C. Gather, "Advances in small lasers," Nat. Photonics **8**, 908–918 (2014).
[47]M. Asada, S. Suzuki, and N. Kishimoto, "Resonant tunneling diodes for sub-terahertz and terahertz oscillators," Jpn. J. Appl. Phys., Part 1 **47**, 4375 (2008).
[48]J. Wang, L. Wang, C. Li, B. Romeira, and E. Wasige, "28 GHz MMIC resonant tunnelling diode oscillator of around 1 mW output power," Electron. Lett. **49**, 816–818 (2013).
[49]B. Romeira, R. Avó, J. Javaloyes, S. Balle, C. Ironside, and J. Figueiredo, "Stochastic induced dynamics in neuromorphic optoelectronic oscillators," Opt. Quantum Electron. **46**, 1391–1396 (2014).
[50]T. Slight, B. Romeira, L. Wang, J. Figueiredo, E. Wasige, and C. Ironside, "A Liénard oscillator resonant tunnelling diode-laser diode hybrid integrated circuit: Model and experiment," IEEE J. Quantum Electron. **44**, 1158–1163 (2008).
[51]B. Romeira, K. Seunarine, C. Ironside, A. Kelly, and J. Figueiredo, "A self-synchronized optoelectronic oscillator based on an RTD photodetector and a laser diode," IEEE Photonics Technol. Lett. **23**, 1148–1150 (2011).
[52]B. Romeira, J. Javaloyes, J. M. L. Figueiredo, C. N. Ironside, H. I. Cantu, and A. E. Kelly, "Delayed feedback dynamics of Lienard-type resonant tunneling-photo-detector optoelectronic oscillators," IEEE J. Quantum Electron. **49**, 31–42 (2013).
[53]C. Mesaritakis, A. Kapsalis, A. Bogris, and D. Syvridis, "Artificial neuron based on integrated semiconductor quantum dot mode-locked lasers," Sci. Rep. **6**, 39317 (2016).
[54]B. Romeira, R. Avó, J. M. L. Figueiredo, S. Barland, and J. Javaloyes, "Regenerative memory in time-delayed neuromorphic photonic resonators," Sci. Rep. **6**, 19510 (2016).
[55]S. Yanchuk and G. Giacomelli, "Spatio-temporal phenomena in complex systems with time delays," J. Phys. A: Math. Theor. **50**, 103001 (2017).
[56]N. Oshima, K. Hashimoto, S. Suzuki, and M. Asada, "Wireless data transmission of 34 Gbit/s at a 500-GHz range using resonant-tunnelling-diode terahertz oscillator," Electronics Letters **52**(22), 1897–1898 (2016).
[57]T. Miyamoto, A. Yamaguchi, and T. Mukai, "Terahertz imaging system with resonant tunneling diodes," Jpn. J. Appl. Phys., Part 1 **55**, 32201 (2016).
[58]N. Kamegai, S. Kishimoto, K. Maezawa, T. Mizutani, H. Andoh, K. Akamatsu, and H. Nakata, "Ultrashort pulse generators using resonant tunneling diodes and their integration with antennas on ceramic substrates," Jpn. J. Appl. Phys., Part 1 **47**, 2833 (2008).
[59]A. Pfenning, F. Hartmann, M. R. S. Dias, F. Langer, M. Kamp, L. K. Castelano, V. Lopez-Richard, G. E. Marques, S. Höfling, and L. Worschech, "Photocurrent-voltage relation of resonant tunneling diode photodetectors," Appl. Phys. Lett. **107**, 81104 (2015).
[60]A. Pfenning, F. Hartmann, F. Langer, M. Kamp, S. Höfling, and L. Worschech, "Sensitivity of resonant tunneling diode photodetectors," Nanotechnology **27**, 355202 (2016).
[61]J. C. Blakesley, P. See, A. J. Shields, B. E. Kardynal, P. Atkinson, I. Farrer, and D. A. Ritchie, "Efficient single photon detection by quantum dot resonant tunneling diodes," Phys. Rev. Lett. **94**, 67401 (2005).
[62]H. W. Li, B. E. Kardynał, D. J. P. Ellis, A. J. Shields, I. Farrer, and D. A. Ritchie, "Quantum dot resonant tunneling diode single photon detector with aluminum oxide aperture defined tunneling area," Appl. Phys. Lett. **93**, 153503 (2008).
[63]Q. Weng, Z. An, B. Zhang, P. Chen, X. Chen, Z. Zhu, and W. Lu, "Quantum dot single-photon switches of resonant tunneling current for discriminating-photon-number detection," Sci. Rep. **5**, 9389 (2015).
[64]M. Nagase, T. Takahashi, and M. Shimizu, "Investigating the bistability characteristics of GaN/AlN resonant tunneling diodes for ultrafast nonvolatile memory," Jpn. J. Appl. Phys., Part 1 **54**, 34201 (2015).
[65]Y. Klofaï, B. Z. Essimbi, and D. Jäger, "An MMIC implementation of FitzHughNagumo neurons using a resonant tunneling diode nonlinear transmission line," Phys. Scr. **90**, 25002 (2015).
[66]B. Romeira, "Dynamics of resonant tunneling diode optoelectronic oscillators," Ph.D. thesis (Universidade do Algarve, 2012).
[67]J. N. Schulman, H. J. De Los Santos, and D. H. Chow, "Physics-based RTD current-voltage equation," IEEE Electron Device Letters **17**(5), 220–222 (1996).
[68]J. K. Hale, *Theory of Functional Differential Equations* (Springer-Verlag, New York, 1977).
[69]A. Lins, W. Melo, and C. Pugh, *On Lienards Equation* (Springer-Verlag, New York, 1977).
[70]J. M. L. Figueiredo, B. Romeira, T. J. Slight, L. Wang, E. Wasige, and C. N. Ironside, "Self-oscillation and period adding from resonant tunnelling diode-laser diode circuit," Electron. Lett. **44**, 876–877 (2008).
[71]B. Romeira, J. M. L. Figueiredo, T. J. Slight, L. Wang, E. Wasige, C. N. Ironside, A. E. Kelly, and R. Green, "Nonlinear dynamics of resonant tunneling optoelectronic circuits for wireless/optical interfaces," IEEE J. Quantum Electron. **45**, 1436–1445 (2009).
[72]B. Romeira, "Synchronisation and chaos in a laser diode driven by a resonant tunnelling diode," IET Optoelectron. **2**, 211–215 (2008).
[73]B. Romeira, J. Figueiredo, C. Ironside, and T. Slight, "Chaotic dynamics in resonant tunneling optoelectronic voltage controlled oscillators," IEEE Photonics Technol. Lett. **21**, 1819–1821 (2009).
[74]J. M. L. Figueiredo, C. N. Ironside, and C. R. Stanley, "Electric field switching in a resonant tunneling diode electroabsorption modulator," IEEE J. Quantum Electron. **37**, 1547–1552 (2001).
[75]I. J. S. Coelho, J. F. Martins-Filho, J. M. L. Figueiredo, and C. N. Ironside, "Modeling of light-sensitive resonant-tunneling-diode devices," J. Appl. Phys. **95**, 8258–8263 (2004).
[76]T. J. Slight and C. N. Ironside, "Investigation into the integration of a resonant tunnelling diode and an optical communications laser: Model and experiment," IEEE J. Quantum Electron. **43**, 580–587 (2007).
[77]C. W. Gardiner, *Handbook of Stochastic Methods*, 2nd ed. (Springer-Verlag, Berlin, 1995).
[78]A. L. Hodgkin and A. F. Huxley, "A quantitative description of membrane current and its application to conduction and excitation in nerve," J. Physiol. **117**, 500–544 (1952).
[79]A. L. Hodgkin, A. F. Huxley, and B. Katz, "Measurement of current-voltage relations in the membrane of the giant axon of loligo," J. Physiol. **116**, 424 (1952).

[80]L. Kuhnert, K. I. Agladze, and V. I. Krinsky, "Image processing using light-sensitive chemical waves," Nature **337**, 244–247 (1989).
[81]F. Pedaci, Z. Huang, M. van Oene, S. Barland, and N. H. Dekker, "Excitable particles in an optical torque wrench," Nat. Phys. **7**, 259–264 (2011).
[82]A. Samardak, A. Nogaret, N. Janson, A. Balanov, I. Farrer, and D. Ritchie, "Spiking computation and stochastic amplification in a neuron-like semiconductor microstructure," J. Appl. Phys. **109**, 102408 (2011).
[83]S. Barbay, R. Kuszelewicz, and A. M. Yacomotti, "Excitability in a semiconductor laser with saturable absorber," Opt. Lett. **36**, 4476–4478 (2011).
[84]D. Goulding, S. P. Hegarty, O. Rasskazov, S. Melnik, M. Hartnett, G. Greene, J. G. McInerney, D. Rachinskii, and G. Huyet, "Excitability in a quantum dot semiconductor laser with optical injection," Phys. Rev. Lett. **98**, 153903 (2007).
[85]F. Selmi, R. Braive, G. Beaudoin, I. Sagnes, R. Kuszelewicz, and S. Barbay, "Relative refractory period in an excitable semiconductor laser," Phys. Rev. Lett. **112**, 183902 (2014).
[86]M. Desroches, J. Guckenheimer, B. Krauskopf, C. Kuehn, H. M. Osinga, and M. Wechselberger, "Mixed-mode oscillations with multiple time scales," SIAM Rev. **54**, 211–288 (2012).
[87]B. Romeira, J. Figueiredo, J. Javaloyes, O. Piro, and S. Balle, "Mixed mode oscillations in a forced optoelectronic circuit for pattern and random bit generation," in Proceedings of the International Conference on Numerical Simulation of Optoelectronic Devices, NUSOD (2014).
[88]F. Leo, S. Coen, P. Kockaert, S.-P. Gorza, P. Emplit, and M. Haelterman, "Temporal cavity solitons in one-dimensional Kerr media as bits in an all-optical buffer," Nat. Photonics **4**, 471–476 (2010).
[89]N. Burić and D. Todorović, "Dynamics of FitzHugh-Nagumo excitable systems with delayed coupling," Phys. Rev. E **67**, 66222 (2003).
[90]G. Stepan, "Delay effects in brain dynamics," Philos. Trans. R. Soc. London, Ser. A **367**, 1059–1062 (2009).
[91]A. M. Yacomotti, G. B. Mindlin, M. Giudici, S. Balle, S. Barland, and J. Tredicce, "Coupled optical excitable cells," Phys. Rev. E **66**, 36227 (2002).
[92]E. Schöll, G. Hiller, P. Hövel, and M. A. Dahlem, "Time-delayed feedback in neurosystems," Philos. Trans. R. Soc. London, Ser. A **367**, 1079–1096 (2009).
[93]B. Kelleher, C. Bonatto, P. Skoda, S. P. Hegarty, and G. Huyet, "Excitation regeneration in delay-coupled oscillators," Phys. Rev. E **81**, 36204 (2010).
[94]L. Weicker, T. Erneux, L. Keuninckx, and J. Danckaert, "Analytical and experimental study of two delay-coupled excitable units," Phys. Rev. E **89**, 12908 (2014).
[95]K. Ikeda, "Multiple-valued stationary state and its instability of the transmitted light by a ring cavity system," Opt. Commun. **30**, 257–261 (1979).
[96]A. Neyer and E. Voges, "Dynamics of electrooptic bistable devices with delayed feedback," IEEE Journal of Quantum Electronics **18**(2), 2009–2015 (1982).
[97]T. Aida and P. Davis, "Oscillation modes of laser diode pumped hybrid bistable system with large delay and application to dynamical memory," IEEE Journal of Quantum Electronics **28**(3), 686–699 (1992).
[98]K. Pyragas, "Continuous control of chaos by self-controlling feedback," Phys. Lett. A **170**, 421–428 (1992).
[99]G. Giacomelli and A. Politi, "Relationship between delayed and spatially extended dynamical systems," Phys. Rev. Lett. **76**, 2686–2689 (1996).
[100]P. B. Umbanhowar, F. Melo, and H. L. Swinney, "Localized excitations in a vertically vibrated granular layer," Nature **382**, 793–796 (1996).
[101]Y. A. Astrov and H.-G. Purwins, "Plasma spots in a gas discharge system: Birth, scattering and formation of molecules," Phys. Lett. A **283**, 349–354 (2001).
[102]K.-J. Lee, W. D. McCormick, J. E. Pearson, and H. L. Swinney, "Experimental observation of self-replicating spots in a reaction-diffusion system," Nature **369**, 215–218 (1994).
[103]J. Wu, R. Keolian, and I. Rudnick, "Observation of a nonpropagating hydrodynamic soliton," Phys. Rev. Lett. **52**, 1421–1424 (1984).
[104]E. Moses, J. Fineberg, and V. Steinberg, "Multistability and confined traveling-wave patterns in a convecting binary mixture," Phys. Rev. A **35**, 2757–2760 (1987).
[105]S. Barland, J. R. Tredicce, M. Brambilla, L. A. Lugiato, S. Balle, M. Giudici, T. Maggipinto, L. Spinelli, G. Tissoni, T. Knodl, M. Miller, and R. Jager, "Cavity solitons as pixels in semiconductor microcavities," Nature **419**, 699–702 (2002).
[106]F. Marino, G. Giacomelli, and S. Barland, "Front pinning and localized states analogues in long-delayed bistable systems," Phys. Rev. Lett. **112**, 103901 (2014).
[107]M. Marconi, J. Javaloyes, S. Balle, and M. Giudici, "How lasing localized structures evolve out of passive mode locking," Phys. Rev. Lett. **112**, 223901 (2014).
[108]B. Garbin, J. Javaloyes, G. Tissoni, and S. Barland, "Topological solitons as addressable phase bits in a driven laser," Nat. Commun. **6**, 5915 (2015).
[109]M. Marconi, J. Javaloyes, S. Barland, S. Balle, and M. Giudici, "Vectorial dissipative solitons in vertical-cavity surface-emitting lasers with delays," Nat. Photonics **9**, 450–455 (2015).
[110]J. Javaloyes, T. Ackemann, and A. Hurtado, "Arrest of domain coarsening via anti-periodic regimes in delay systems," Phys. Rev. Lett. **115**, 203901 (2015).
[111]P. Coullet, C. Riera, and C. Tresser, "A new approach to data storage using localized structures," Chaos **14**, 193–198 (2004).
[112]K. Engelborghs, T. Luzyanina, and D. Roose, "Numerical bifurcation analysis of delay differential equations using dde-biftool," ACM Trans. Math. Software **28**, 1–21 (2002).
[113]P. Camelin, J. Javaloyes, M. Marconi, and M. Giudici, "Electrical addressing and temporal tweezing of localized pulses in passively-mode-locked semiconductor lasers," Phys. Rev. A **94**, 063854 (2016).